

A Luminosity Function of Ly α -Emitting Galaxies at $z \approx 4.5$ ^{1,2}

Steve Dawson³, James E. Rhoads⁴, Sangeeta Malhotra⁴, Daniel Stern⁵, JunXian Wang⁶,
Arjun Dey⁷, Hyron Spinrad³, Buell T. Jannuzi⁷

ABSTRACT

We present a catalog of 59 $z \approx 4.5$ Ly α -emitting galaxies spectroscopically confirmed in a campaign of Keck/DEIMOS follow-up observations to candidates selected in the Large Area Lyman Alpha (LALA) narrow-band imaging survey. We targeted 97 candidates for spectroscopic follow-up; by accounting for the variety of conditions under which we performed spectroscopy, we estimate a selection reliability of $\sim 76\%$. Together with our previous sample of Keck/LRIS confirmations, the 59 sources confirmed herein bring the total catalog to 73 spectroscopically confirmed $z \approx 4.5$ Ly α -emitting galaxies in the ≈ 0.7 degrees² covered by the LALA imaging. As with the Keck/LRIS sample, we find that a non-negligible fraction of the confirmed Ly α lines have rest-frame equivalent widths ($W_{\lambda}^{\text{rest}}$) which exceed the maximum predicted for normal stellar populations: 17% – 31% (93% confidence) of the detected galaxies show $W_{\lambda}^{\text{rest}} > 190 \text{ \AA}$, and 12% – 27% (90% confidence) show $W_{\lambda}^{\text{rest}} > 240 \text{ \AA}$. We construct a luminosity

¹ Based in part on observations made at the W.M. Keck Observatory, which is operated as a scientific partnership among the California Institute of Technology, the University of California, and the National Aeronautics and Space Administration. The Observatory was made possible by the generous financial support of the W.M. Keck Foundation.

²Our data were obtained using community access telescope time made available under the National Science Foundation's Telescope System Instrumentation Program (TSIP), awarded by the National Optical Astronomy Observatory.

³ Department of Astronomy, University of California at Berkeley, Mail Code 3411, Berkeley, CA 94720 USA; sdawson@astro.berkeley.edu, spinrad@astro.berkeley.edu

⁴ Arizona State University, Department of Physics and Astronomy Arizona State University, P.O. Box 871504 Tempe, Arizona 85287-1504; Sangeeta.Malhotra@asu.edu, James.Rhoads@asu.edu

⁵ Jet Propulsion Laboratory, California Institute of Technology, Mail Stop 169-527, Pasadena, CA 91109 USA; stern@zwoelfkinder.jpl.nasa.gov.

⁶ Center for Astrophysics, University of Science and Technology of China, Hefei, Anhui 230026, China; jxw@ustc.edu.cn

⁷ KPNO/NOAO, 950 N. Cherry Ave., P.O. Box 26732, Tucson, AZ 85726 USA; dey@noao.edu, jannuzi@noao.edu

function of $z \approx 4.5$ Ly α emission lines for comparison to Ly α luminosity functions spanning $3.1 < z < 6.6$. We find no significant evidence for Ly α luminosity function evolution from $z \approx 3$ to $z \approx 6$. This result supports the conclusion that the intergalactic medium remains largely reionized from the local universe out to $z \approx 6.5$. It is somewhat at odds with the pronounced drop in the cosmic star formation rate density recently measured between $z \sim 3$ and $z \sim 6$ in continuum-selected Lyman-break galaxies, and therefore potentially sheds light on the relationship between the two populations.

Subject headings: cosmology: observations — early universe — galaxies: evolution — galaxies: formation — galaxies: high-redshift

1. Introduction

Observational cosmology has recently witnessed a tremendous increase in proficiency in the identification of galaxies at the earliest cosmic epochs. Thanks in large part to the availability of large-format mosaic CCDs well-suited for wide-field imaging and spectroscopic multiplexing, we are now transitioning from exotic, single detections of high-redshift galaxies (e.g., Dey et al. 1998; Weymann et al. 1998; Ellis et al. 2001; Ajiki et al. 2002; Dawson et al. 2002; Hu et al. 2002; Cuby et al. 2003; Taniguchi et al. 2003; Nagao et al. 2004; Rhoads et al. 2004; Stern et al. 2005) to the assembly of statistically robust samples spanning the earliest accessible redshifts. Robust samples of this kind are necessary for understanding the systematics of selection criteria, and of the spatial distribution of the galaxies themselves. Deficiencies in such understanding are the main source of uncertainty in inferred luminosity functions and universal star formation rates, which in turn are the keys to understanding the cosmic history of star formation, galaxy assembly and evolution, and even the early ionization history of the IGM (e.g., Malhotra & Rhoads 2004; Stern et al. 2005).

Searches for high-redshift galaxies typically follow the by-now familiar strategy of targeting redshifted Ly α emission at increasing wavelengths with narrow-band imaging in windows of low night-sky emission (e.g., Cowie & Hu 1998; Hu et al. 1998; Rhoads et al. 2000; Kodaira et al. 2003; Maier et al. 2003; Hu et al. 2004; Taniguchi et al. 2005), or by photometric selection in broad-band imaging of the redshifted Lyman break (e.g., Steidel et al. 1996; Madau et al. 1996; Lowenthal et al. 1997; Spinrad et al. 1998; Lehnert & Bremer 2003; Ando et al. 2004; Bouwens et al. 2004; Dickinson et al. 2004; Ouchi et al. 2004; Stanway et al. 2004a,b; Yan & Windhorst 2004). These two techniques are complementary; Ly α searches at typical sensitivities can identify galaxies with UV-continua too faint to be detected by the Lyman break method, but such surveys only select that fraction of galaxies with strong

line emission.

The Large Area Lyman Alpha (LALA) survey (Rhoads et al. 2000) has recently identified in deep narrow-band imaging a large sample of Ly α -emitting galaxies at redshifts $z \approx 4.5$ (Malhotra & Rhoads 2002), $z \approx 5.7$ (Rhoads & Malhotra 2001; Rhoads et al. 2003), and $z \approx 6.5$ (Rhoads et al. 2004). In Dawson et al. 2004 (Paper I), we reported on the spectroscopic confirmation with the W. M. Keck Observatory’s Low Resolution Imaging Spectrometer (LRIS; Oke et al. 1995) of 17 Ly α -emitting galaxies selected in the LALA $z \approx 4.5$ survey. The resulting sample of confirmed Ly α emission lines showed large equivalent widths (median $W_{\lambda}^{\text{rest}} \approx 80 \text{ \AA}$) but narrow velocity widths (FWHM $\Delta v < 500 \text{ km s}^{-1}$), indicating that the Ly α emission in these sources derives from star formation, not from AGN activity. Models of star formation in the early universe predict that a small fraction of Ly α -emitting galaxies at $z \approx 4.5$ may be nascent, metal-free objects (e.g., Scannapieco et al. 2003), and indeed we found with 90% confidence that 3 to 5 of the confirmed sources exceed the maximum Ly α equivalent width predicted for normal stellar populations. However, we did not detect the He II $\lambda 1640$ emission expected to be characteristic of primordial star formation. Specifically, the He II $\lambda 1640$ flux in a composite of the 11 highest resolution spectra in the Keck/LRIS sample was formally consistent with zero, with a 2σ (3σ) upper limit of 13% (20%) of the flux in the Ly α line. In other words, though these galaxies may be young, they show no evidence of being truly primitive, Population III objects.

We have recently more than quadrupled our catalog of spectroscopically-confirmed Ly α -emitting galaxies at $z \approx 4.5$ with a spectroscopic campaign using the W. M. Keck Observatory’s DEep IMaging Multi-object Spectrograph (DEIMOS; Faber et al. 2003), targeting candidates selected from the LALA survey. Together with the detections presented in Paper I (and accounting for minor overlap in the samples), the 59 Ly α -emitters confirmed with Keck/DEIMOS bring the total catalog to 73 spectroscopically confirmed $z \approx 4.5$ Ly α -emitting galaxies in the $\approx 0.7 \text{ degrees}^2$ imaged by LALA. In this paper, we utilize these additional confirmations to update the results of Paper I, and to construct a luminosity function of $z \approx 4.5$ Ly α emission lines for comparison to Ly α luminosity functions spanning $3.1 < z < 6.6$. We describe our imaging and spectroscopic observations in § 2, and we summarize the results of the spectroscopic campaign in § 3. In § 4, we investigate the distribution of the Ly α lines in equivalent width, we construct Ly α luminosity functions for our sample and for several extant samples, and we discuss the implications of the luminosity functions for the relationship between Ly α -emitters and Lyman-break galaxies (LBGs), and for the history of reionization. Throughout this paper we adopt a Λ -cosmology with $\Omega_{\text{M}} = 0.3$ and $\Omega_{\Lambda} = 0.7$, and $H_0 = 70 \text{ km s}^{-1} \text{ Mpc}^{-1}$ (Spergel et al. 2003). At $z = 4.5$, such a universe is 1.3 Gyr old, the lookback time is 90.2% of the total age of the Universe, and an angular size of $1''.0$ corresponds to 6.61 comoving kpc.

2. Observations

2.1. Narrow-Band and Broad-Band Imaging

The LALA survey concentrates on two primary fields, “Boötes” (14:25:57 +35:32; J2000.0) and “Cetus” (02:05:20 –04:55; J2000.0). Each field is 36×36 arcminutes in size, corresponding to a single field of the 8192×8192 pixel Mosaic CCD cameras on the 4m Mayall Telescope at Kitt Peak National Observatory and on the 4m Blanco Telescope at Cerro Tololo Inter-American Observatory. The $z \approx 4.5$ search uses five overlapping narrow-band filters each with full width at half maximum (FWHM) $\approx 80 \text{ \AA}$ (Figure 1). The central wavelengths are 6559, 6611, 6650, 6692, and 6730 \AA , giving a total redshift coverage of $4.37 < z < 4.57$ and a survey volume of 7.4×10^5 comoving Mpc^3 per field. In roughly 6 hours per filter per field, we achieve 5σ line detections in $2''.3$ apertures of $\approx 2 \times 10^{-17} \text{ erg cm}^{-2} \text{ s}^{-1}$.

The primary LALA survey fields were chosen to lie within the NOAO Deep Wide-Field Survey (NDWFS; Jannuzi & Dey 1999). Thus, deep NDWFS broad-band images are available in a custom B_W filter ($\lambda_0 = 4135 \text{ \AA}$, FWHM = 1278 \AA ; Jannuzi & Dey 1999, Jannuzi et al., in preparation) and in the Harris set Kron-Cousins R and I , as well as J , H , K , and K_s . The LALA Boötes field benefits from additional deep V and SDSS z' filter imaging. The imaging data reduction is described in Rhoads et al. (2000), and the candidate selection is described in Rhoads & Malhotra (2001) and Malhotra & Rhoads (2002). Briefly, candidates are selected based on a 5σ detection in a narrow-band filter, the flux density of which must be twice the R -band flux density, and must exceed the R -band flux density at the 4σ confidence level. To guard against foreground interlopers, we require an observed equivalent width $W_\lambda^{\text{obs}} > 80 \text{ \AA}$, and a non-detection in the B_W band (at the $< 2\sigma$ level).

2.2. Spectroscopic Observations

Between 2003 March and 2004 May we obtained spectroscopy of 97 $z \approx 4.5$ candidate Ly α -emitters with the DEep IMaging Multi-object Spectrograph (DEIMOS; Faber et al. 2003), a second-generation camera on the Keck II telescope with high multiplexing capabilities and improved red sensitivity. Each slitmask included approximately 15 candidate Ly α -emitters (mixed in with roughly 50 other spectroscopic targets) and was observed for 1.5 to 2.0 hrs in 0.5 hr increments. Six slitmasks targeting a total of 80 candidates were observed in the Boötes field; the airmass in these observations never exceeded 1.5. One slitmask targeting 17 candidates was observed in the Cetus field; the airmass for this slitmask was constrained to less than 1.8. The seeing in all observations ranged from $0''.5$ to $1''.0$. We

estimated the seeing by examining the alignment stars observed during the direct-imaging phase of setting up the slitmask; that is, the stars were imaged through the BAL12 (clear) filter with the grating angle set such that zero-order light fell on the detector.

All observations employed 1''0 wide slitlets and the 600ZD grating ($\lambda_{\text{blaze}} = 7500 \text{ \AA}$; $0.65 \text{ \AA pixel}^{-1}$ dispersion; $\Delta\lambda_{\text{FWHM}} \approx 4.5 \text{ \AA} \approx 200 \text{ km s}^{-1}$)¹. The wavelength range covered by a typical slitlet was roughly $5000 \text{ \AA} \lesssim \lambda \lesssim 10000 \text{ \AA}$. The precise wavelength coverage depended somewhat on the location of the slitlet on the slitmask, but never exceeded 4390 \AA at the low extremum or $1.1 \text{ }\mu\text{m}$ at the high extremum. No order-blocking filter was used; since the targets were primarily selected to have red colors, second order light should not be of concern. Most nights suffered from some cirrus; relative flux calibration was achieved from observations of standard stars from Massey & Gronwall (1990) observed during the same observing run. It should also be noted that the position angle of an observation was set by the desire to maximize the number of targets on a given slitmask, so observations were generally not made at the parallactic angle.

We processed the two-dimensional data using the DEEP2 DEIMOS pipeline². We performed small (0''.5) dithers between exposures on our initial observing run; to reduce these data, we supplemented the DEEP2 DEIMOS pipeline with additional home-grown routines. We extracted spectra with the IRAF³ package (Tody 1993) using the optimal extraction algorithm (Horne 1986), following standard slit spectroscopy procedures.

Prior experience with faint-object spectroscopy dictates that a small but significant error in the measured flux of faint continua may be introduced by sky subtraction during the processing of the two-dimensional spectra. We investigated this possibility with ~ 10 additional non-overlapping extractions in source-free regions in each two-dimensional spectrum, parallel to and along the same trace as the extraction of the neighboring Ly α -emitting galaxy. We then fitted these blank-sky spectra over the same region that we fitted for the continuum redward and blueward of the emission line in the object extraction. For 15 sources, these fits yielded a tiny residual signal, which we interpreted as a systematic error in the

¹We measured the instrumental resolution by autocorrelating one-dimensional extracted spectra of night-sky emission lines. The autocorrelation results in an effective average line profile with a high signal-to-noise ratio, which we fit with a Gaussian to obtain the FWHM. We performed this test on ~ 50 night-sky spectra with the result $\Delta\lambda_{\text{FWHM}} = 4.47 \pm 0.03 \text{ \AA}$. The quoted uncertainty is the error in the mean, and does not include possible systematic effects due to blended night sky lines.

²See <http://astron.berkeley.edu/~cooper/deep/spec2d/>

³IRAF is distributed by the National Optical Astronomy Observatory, which is operated by the Association of Universities for Research in Astronomy, Inc., under cooperative agreement with the National Science Foundation.

two-dimensional sky subtraction and applied as a correction to quantities derived from the object spectra. The typical correction was $\sim 0.04 \pm 0.02 \mu\text{Jy}$, but the correction reached as high as $\sim 0.1 \pm 0.07 \mu\text{Jy}$ in three cases. Sky-subtraction residuals of this kind generally resulted when a small spectroscopic slit contained a bright serendipitous detection in addition to the target, the combination of which made it difficult to fit the sky background.

3. Spectroscopic Results

Out of 97 spectroscopic candidates, we achieved 73 detections, 59 of which constitute Ly α confirmations according to the criteria outlined below. A histogram of these confirmations appears in Figure 1, and a set of sample spectra are shown in Figure 2. The spectroscopic properties of the Ly α confirmations are summarized in Table 1. One detected galaxy lacks an emission line but shows a large spectral discontinuity identified as the onset of foreground Ly α -forest absorption at $z = 4.462^4$. Three of the detections are identifiably low-redshift interlopers (two resolved [O II] $\lambda 3727$ doublets at $z \sim 0.8$; one complex of [O III] $\lambda\lambda 4959, 5007$ and H β at $z \sim 0.3$) which survived the candidate selection thanks to their unusually high equivalent widths (e.g., $W_{\lambda}^{\text{obs}} > 2000 \text{ \AA}$). In ten cases, we see a possible low signal-to-noise ratio ($\lesssim 1$) emission line located at the correct location in both wavelength space and physical position to be associated with the narrow-band selected target. However, even if these “detections” are real, they cannot be reliably identified as either Ly α or as low-redshift interlopers. If these 10 cases were in fact low signal-to-noise ratio detections of Ly α emission, then the “success rate” of the Keck/DEIMOS campaign would be 72%, identical to that of the Keck/LRIS sample described in Paper I (but also subject to all the caveats listed therein). We do not include unconfirmed sources in any of the ensuing discussion.

The remaining 24 targets were classified as nondetections. Five of these slitlets suffered from some kind of instrument or reduction issue, e.g., the target was dithered off the slitlet and so did not reproduce across the individual integrations, or irregularities in the machining of the slitmask resulted in defects in the data processing. Of the final 19 nondetections, 13 targets were observed under adverse conditions (e.g., variable cloud coverage, and/or poor seeing) for which the general spectroscopic yield was low. Our failure to confirm these targets as $z \approx 4.5$ Ly α -emitters should not be taken to bear on the efficacy of candidate selection.

⁴A sufficiently bright Lyman break galaxy can be selected as a narrowband excess object when the narrow filter lies redward of the Ly α forest, so that neutral hydrogen absorption significantly reduces the broad band flux without affecting the narrow band flux.

Six nondetections were observed under photometric conditions with subarcsecond seeing for which the spectroscopic yield was otherwise high. However, subsequent inspection of the imaging revealed that five of these targets were suboptimal candidates for one of a variety of reasons: two candidates sit on weak satellite trail residuals; one candidate appears in an initial epoch of imaging but not in subsequent epochs, suggesting that it is a variable source or a spurious detection; two candidates are marginal or irregular detections in the imaging. This leaves just one otherwise viable candidate Ly α -emitter that was not confirmed in spectroscopy, even though the conditions for spectroscopy were favorable. Since this source (J1424398+353801) was a single-band detection in the narrow-band imaging, it is possible that it represents a spurious false-positive and not a genuine candidate. Given the large number ($10^{6.5}$) of independent resolution elements in the images, we expect about one false-positive at the 5σ -level per LALA field per narrow-band filter, and this number could be larger if the noise properties of the image are not precisely Gaussian (see Rhoads et al. 2003).

To estimate the reliability of our candidate selection, we consider only the foregoing six non-detections, the three low-redshift interlopers, and the 10 low signal-to-noise ratio detections as legitimate non-confirmations. This admittedly rough scheme suggests a rate of 59 detections out of 78 viable candidates observed spectroscopically under workable conditions, for a final selection reliability of $\sim 76\%$. The rate of spectroscopic confirmation is plotted as a function of narrow-band flux in Figure 3.

3.1. Spectroscopic Sensitivity to Ly α Emission

We now assess our spectroscopic sensitivity to line emission. Each one-dimensional spectrum was created with a variance-weighted optimal extraction (Horne 1986) from the two-dimensional data. For each object, we therefore have both the flux and the flux variance as a function of wavelength. We used the variance spectrum to estimate the uncertainties in quantities derived from the object spectra, e.g., we sum the variance spectrum in quadrature over the wavelength range covered by the observed line profile to estimate the uncertainty in the measured line flux. However, the variance may also be used to measure the noise over wavelength ranges corresponding to any Ly α line we *might* have detected given the redshift range permitted by our narrow-band imaging, roughly $4.37 < z < 4.57$. Accordingly, for each object we ranged over redshift and calculated the smallest emission line flux detectable:

$$F_{\text{lim}}(z) = n_{\text{sig}} \delta_{\text{disp}} \left\{ \sum_{\lambda=\lambda_1(z)}^{\lambda_2(z)} \sigma_{\lambda}^2 \right\}^{\frac{1}{2}}, \quad (1)$$

where n_{sig} is the minimum signal-to-noise ratio necessary for a detection (here taken to be 3), δ_{disp} is the grating dispersion ($0.63 \text{ \AA pix}^{-1}$ for the Keck/DEIMOS 600ZD grating), and σ_{λ} is the flux error in each pixel determined during the variance-weighted one-dimensional extraction, in units of f_{λ} . The limits λ_1 and λ_2 are defined by

$$\begin{aligned}\lambda_1(z) &= (1+z)(1216 - \Delta\lambda/2) , \\ \lambda_2(z) &= (1+z)(1216 + \Delta\lambda/2) ,\end{aligned}\tag{2}$$

where $\Delta\lambda$ is the fiducial rest-frame full width of the emission line (here taken to be 3 \AA).

We assembled the $F_{\text{lim}}(z)$ for each object into a grid and then ranked the F_{lim} at each redshift, resulting in the cumulative distribution of sensitivity to $\text{Ly}\alpha$ emission line flux shown in Figure 4. The distribution may be interpreted as giving the probability that a putative $\text{Ly}\alpha$ emission line of a given flux and a given redshift would have been detected in our spectroscopic campaign. Since we cover a comparatively small redshift range centered essentially at the peak of the detector throughput, the sensitivity distribution is dominated entirely by night-sky emission lines rather than by instrumental effects. And since the original narrow-band survey was designed to probe relatively noise-free windows in night-sky emission, the spectroscopic sensitivity is fairly flat over the redshift range of interest. In sum, the implied depth of our spectroscopic survey is 50% complete to $f(\text{Ly}\alpha) \sim 3 \times 10^{-18} \text{ erg cm}^{-2} \text{ s}^{-1}$, approximately 7 times deeper than the narrow-band imaging. Note that because we derived this sensitivity function from the sample of spectra themselves, it depends entirely on the details governing the manner in which these spectra were obtained and processed, and is therefore valid for this survey only.

3.2. Redshift Identification

Of course, given the detection of an emission line, the identification of that line as high-redshift $\text{Ly}\alpha$ can remain problematic. Thorough treatments of the pitfalls of one-line redshift identifications are given elsewhere (e.g., Stern & Spinrad 1999; Stern et al. 2000; Dawson et al. 2001). In surveys of the present kind, the primary threat to the proper interpretation of a solo emission line is the potential for low-redshift, high-equivalent width [O II] $\lambda 3727$ to survive candidate selection, and then to be misidentified as high-redshift $\text{Ly}\alpha$ in later spectroscopy. However, at $z = 0.8$ (the redshift of an [O II] $\lambda 3727$ line mistaken for $\text{Ly}\alpha$ at $z = 4.5$), the redshifted separation between the individual lines of the [O II] $\lambda 3727$ doublet (rest wavelengths 3726 \AA and 3729 \AA , respectively) is 5.4 \AA . The doublet is therefore just resolved in our spectroscopy and serves to uniquely flag [O II] $\lambda 3727$ interlopers (Figure 5); this is an improvement afforded by Keck/DEIMOS over the spectroscopy presented in Paper I. Less frequently, high-equivalent width [O III] $\lambda 5007$ survives as an interloper in

our candidate selection. However, [O III] $\lambda 5007$ can typically be identified by neighboring [O III] $\lambda 4959$ at one-third its strength, or by neighboring H β .

Beyond merely eliminating plausible low-redshift interlopers, we may identify Ly α emission by its characteristically asymmetric morphology, or by the presence of a continuum break if the continuum is sufficiently well-detected. Each of our confirmed Ly α detections demonstrates the asymmetric emission line profile characteristic of the line, where neutral hydrogen outflowing from an actively star-forming galaxy imposes a sharp blue cutoff and broad red wing (e.g., Dey et al. 1998; Stern & Spinrad 1999; Manning et al. 2000; Dawson et al. 2002; Rhoads et al. 2003; Hu et al. 2004; Stern et al. 2005; Taniguchi et al. 2005). In Figure 6, we present a scatter plot of the flux-based asymmetry statistic:

$$a_f = \frac{\int_{\lambda_p}^{\lambda_{10,r}} f_\lambda d\lambda}{\int_{\lambda_{10,b}}^{\lambda_p} f_\lambda d\lambda}, \quad (3)$$

versus the wavelength-based asymmetry statistic:

$$a_\lambda = \frac{(\lambda_{10,r} - \lambda_p)}{(\lambda_p - \lambda_{10,b})}, \quad (4)$$

for our sample, where λ_p is the wavelength of the peak of the emission line, and $\lambda_{10,b}$ and $\lambda_{10,r}$ are the wavelengths at which the line flux first exceeds 10% of the peak on the blue side and on the red side of the emission line, respectively (see Rhoads et al. 2003, 2004, and Paper I)⁵. Each of the confirmed Ly α emitters in this sample satisfies $a_f > 1.0$ or $a_\lambda > 1.0$, and 52 out of 59 sources satisfy both. As we found for the lower resolution Keck/LRIS sample in Paper I, the present Ly α sample, observed with higher spectral resolution using Keck/DEIMOS, is systematically segregated from low-redshift [O II] $\lambda 3727$ in a_f - a_λ space.

As a final diagnostic, we note that in each of our confirmed Ly α -emitters for which the continuum is sufficiently well-detected, the spectrum shows a continuum decrement consistent with the onset of absorption by the Ly α forest at $\lambda_{\text{rest}} = 1216 \text{ \AA}$. The break amplitude is typically characterized by $1 - f_\nu^{\text{short}}/f_\nu^{\text{long}}$, where we define f_ν^{short} as the variance-weighted flux density in a 1200 \AA window beginning 30 \AA below the emission line; f_ν^{long} is the same, but above the emission line. In the 24 sources for which f_ν^{long} is detected to better than 2σ , all but two sources have $1 - f_\nu^{\text{short}}/f_\nu^{\text{long}} > 0.5$, consistent with continuum break amplitudes at

⁵As in Paper I, the error bars on a_λ and a_f were determined with Monte Carlo simulations in which we modeled each emission line with the truncated Gaussian profile described in Hu et al. (2004) and Rhoads et al. (2004), added random noise in each pixel according to the photon counting errors, and measured the widths $\sigma(a_\lambda)$ and $\sigma(a_f)$ of the resulting distributions of a_λ and a_f for the given line. That is, for each $a_{\lambda,i}$, the error $\delta a_{\lambda,i} = \sigma(a_{\lambda,i})$, and similarly for each $a_{f,i}$.

$z = 4.5$ in theoretical models (e.g., Madau 1995; Zhang et al. 1997), in the lower resolution Keck/LRIS sample presented in Paper I, and in other similar datasets (see Stern & Spinrad 1999, and references therein).

4. Discussion

Together with the observations presented in Paper I (and accounting for minor overlap in the samples), the 59 Ly α -emitters confirmed herein bring the total catalog of spectroscopically confirmed $z \approx 4.5$ Ly α -emitting galaxies to 73 objects in the ≈ 0.7 degrees² surveyed by the LALA imaging. We now update the characteristics of this population as they were estimated in Paper I by investigating the distribution of the total sample in equivalent width. We then construct a $z \approx 4.5$ Ly α luminosity function, carefully accounting for survey incompleteness and for spectroscopic sensitivity, and we compare the result to Ly α luminosity functions spanning $3.1 < z < 6.6$.

4.1. The Equivalent Width Distribution

As in Paper I, we determine the rest-frame equivalent widths directly from the spectra according to $W_{\lambda}^{\text{rest}} = (F_{\ell}/f_{\lambda,r})/(1+z)$, where F_{ℓ} is the flux in the emission line and $f_{\lambda,r}$ is the measured red-side continuum flux density. The resulting equivalent width distribution is plotted in Figure 7, together with the equivalent widths measured in Paper I.

Before interpreting this distribution, one should be cautioned that the $W_{\lambda}^{\text{rest}}$ determination is very sensitive to uncertainty in the measured continuum. Since the continuum estimate enters into the denominator of the expression for $W_{\lambda}^{\text{rest}}$, the characteristically small continuum values and their large fractional uncertainties cause significant scatter in the measurement, and the resulting error is neither Gaussian nor symmetric about the measured value. Especially problematic is the fact that the largest values of $W_{\lambda}^{\text{rest}}$ are also the least certain. Detailed discussions of the uncertainties in measuring $W_{\lambda}^{\text{rest}}$ in high-redshift Ly α -emitters, along with the complicating effects of dust content, gas kinematics, and intergalactic absorption, are given in Hu et al. (2004) and in Paper I.

With these caveats in mind, we rigorously treated the error bars on the equivalent width estimates, and we restricted the analysis to sources with red-side continuum signal-to-noise ratios $\gtrsim 1$. To determine the equivalent width error bars, we first associated each measured line flux $F_{\ell,i} \pm \delta F_{\ell,i}$ with a Gaussian probability density function (PDF) centered on $F_{\ell,i}$ with width $\sigma = \delta F_{\ell,i}$; we proceeded similarly for the measured continuum fluxes. We then

generated a grid of line flux versus continuum flux on which each node has an associated equivalent width and is assigned a weight given by the probability distribution on each of its flux axes. Next we collapsed the grid into a histogram of equivalent widths, adding the weight from each grid point to the appropriate equivalent width bin. The result is a non-Gaussian PDF $P_i(w)$ for which $P_i(w) dw$ is the probability of observing $W_{\lambda,i}^{\text{rest}}$ in the interval $w < W_{\lambda,i}^{\text{rest}} < w + dw$. The error bars δw_+ and δw_- are then 1σ confidence intervals determined by integrating over the probability density functions $P_i(w)$. They are symmetric in probability density-space in the sense that $\int_{w-\delta w_-}^w P_i(w') dw' = \int_w^{w+\delta w_+} P_i(w') dw' = 0.34$.

We find the resulting distribution to be broadly consistent with the equivalent widths presented in Fujita et al. (2003) for $z \sim 3.7$ and in Hu et al. (2004) for $z \sim 5.7$. While the majority of sources can be understood as comparatively young (1 to 10 Myr) galaxies with Salpeter initial mass functions (IMFs), a non-negligible fraction exceeds the largest rest-frame equivalent widths expected from such stellar populations. Malhotra & Rhoads (2002) use a Salpeter initial mass function, an upper mass cutoff of $120 M_\odot$, and a metallicity of 1/20th solar to find maximum Ly α equivalent widths of 300 Å, 150 Å, and 100 Å for stellar populations of ages 10^6 , 10^7 , and 10^8 years, respectively. Adopting a correction factor of 0.64 as an upper limit to the effect of IGM absorption on the measurement of W_λ^{rest} in spectroscopy effectively reduces these upper limits to 190 Å, 100 Å, and 60 Å (see discussion in Paper I). Owing to the lower metallicity used in their models, the pre-IGM-corrected values of Malhotra & Rhoads (2002) are slightly higher than the canonical limiting Ly α rest-frame equivalent width of 240 Å given by Charlot & Fall (1993).

Using the ensemble of $P_i(w)$ described above, we find that 12% – 27% (90% confidence) of the galaxies in this sample show $W_\lambda^{\text{rest}} > 240$ Å, and 17% – 31% (93% confidence) show $W_\lambda^{\text{rest}} > 190$ Å. Both results are nearly identical to the values given in Paper I. On the simplest interpretation, these galaxies are required to be very young (age $< 10^6$ years), or to have IMFs skewed in favor of the production of massive stars. The possibility that AGNs in our sample are producing stronger-than-expected Ly α emission seems unlikely due to the comparatively narrow velocity widths of the Ly α lines and to the absence of the high-ionization state UV emission lines symptomatic of AGN activity. Moreover, deep (~ 170 ks) *Chandra*/ACIS imaging of LALA $z \approx 4.5$ candidates in both Boötes (Malhotra et al. 2003) and in Cetus (Wang et al. 2004) resulted in X-ray non-detections to an average 3σ limiting luminosity of $L_{2-8\text{keV}} < 2.8 \times 10^{42} \text{ erg s}^{-1}$. This limit is roughly an order of magnitude fainter than what is typically observed for even the heavily obscured, Type II AGNs (e.g., Stern et al. 2002; Norman et al. 2002; Dawson et al. 2003). By comparing the upper limit on the typical X-ray to Ly α luminosity ratio for the Ly α galaxy sample to the observed values of this ratio for quasar and Seyfert galaxy samples, Malhotra et al. (2003) and Wang et al. (2004) conclude that AGN account for $\lesssim 5\%$ of the Ly α galaxy sample.

4.2. Empirical Cumulative Luminosity Function

In Figure 8, we present an empirical cumulative Ly α line luminosity function computed for our sample at $z \sim 4.5$ and compare this to luminosity functions computed for several other samples spanning $3.1 < z < 6.6$. The cumulative luminosity function gives for each Ly α line luminosity $L(\text{Ly}\alpha)$ the total number density of Ly α lines brighter than $L(\text{Ly}\alpha)$. The comparison samples are drawn from spectroscopic follow-up of narrow-band surveys with roughly comparable flux limits and candidate-selection criteria (except where noted, below). We do not include non-spectroscopic Ly α -emitter luminosity functions (e.g., Ouchi et al. 2003) among the comparison samples. In each case, we converted the reported Ly α line fluxes to line luminosities using a Λ -cosmology with $\Omega_{\text{M}} = 0.3$ and $\Omega_{\Lambda} = 0.7$, and $H_0 = 70 \text{ km s}^{-1} \text{ Mpc}^{-1}$, and we made a minimal attempt to account for incompleteness⁶. Specifically, the volume from which Ly α -emitting candidates were selected by their narrow-band excess is simply defined by the solid angle covered by the narrow-band imaging and the redshift range allowed by the narrow-band filter. However, the *effective* volume surveyed by the spectroscopic follow-up is smaller than the imaging survey volume by a factor of $N_{\text{spec}}/N_{\text{cand}}$, where N_{cand} is the total number of Ly α -emitting candidates discovered in the imaging, and N_{spec} is the number of candidates actually targeted for spectroscopy. We estimated the uncertainties in the cumulative luminosity functions with Monte Carlo simulations. Assuming the errors in the Ly α line fluxes are Gaussian, we created synthetic data sets by drawing randomly from the Gaussian Ly α flux PDFs for each object in each sample. The result for each sample was then a distribution of cumulative luminosity functions, which may be used to define upper and lower confidence intervals. Figure 8 depicts 95% confidence intervals; where more than one survey is plotted, just the confidence intervals for the survey with the largest range in line fluxes is depicted.

No strong evolution is readily evident in the cumulative Ly α luminosity functions between $z \sim 3$ and $z \sim 6$. The only significant scatter between luminosity functions occurs between the various $z \sim 3$ surveys, and that scatter likely finds its origin in differences in the manner in which the experiments were performed. Foremost, the area surveyed by the Cowie & Hu (1998) effort is comparatively small: just 25 arcmin^2 in each of two fields (HDF and SSA 22), as opposed to 300 arcmin^2 in Kudritzki et al. (2000) and 132 arcmin^2 in Fujita et al. (2003). Cowie & Hu (1998) note that the number counts in their HDF field appears to be 2.5 times richer in narrow-band excess objects than their SSA 22 field, highlighting the susceptibility of small survey areas to cosmic variance. Separately, as noted by

⁶Hu et al. (2004) provide fluxes for their $z \sim 5.7$ sources as measured in narrow-band imaging, rather than Ly α line fluxes as measured in spectroscopy. As such, we adopt the conversion given in Stern et al. (2005) to estimate $f_{\text{Ly}\alpha}$ from f_{ν}^{NB} .

Hu et al. (2004), the Fujita et al. (2003) data may comparatively under-represent the density of Ly α -emitters due to their more stringent equivalent width criterion of $W_{\lambda}^{\text{obs}} > 250$ Å, as opposed to $W_{\lambda}^{\text{obs}} > 77$ Å in Cowie & Hu (1998) and effectively $W_{\lambda}^{\text{obs}} \gtrsim 100$ Å in Kudritzki et al. (2000).

4.3. The V/V_{max} Estimate

We now perform a more rigorous measurement of the $z \approx 4.5$ Ly α luminosity function using a modified version of the V/V_{max} method (e.g., Hogg et al. 1998; Fan et al. 2001). For each galaxy, V_{max} is the volume over which Ly α of a given luminosity could be located and still be detected by our survey; the luminosity function is then the sum of the inverse volumes of all galaxies in the given luminosity bins. Our modifications to the V/V_{max} method account for incompleteness in two senses. First, not every galaxy candidate identified in imaging was targeted in follow-up spectroscopy. Following Hogg et al. (1998), Figure 9 shows the fraction of narrow-band selected candidate Ly α -emitters which were targeted for spectroscopy as a function of flux in the band in which the candidate was detected. We label this *a priori* completeness function η_{try} ; the candidate Ly α flux $f_{\text{Ly}\alpha}$ can be roughly estimated from the flux in the narrow-band f_{ν}^{NB} with $f_{\text{Ly}\alpha} = w_n(f_{\nu}^{\text{NB}} - f_{\nu}^{\text{R}})$, where w_n is the width of the narrow-band filter and f_{ν}^{R} is the flux of the candidate in the R -band.

Second, even if a candidate Ly α -emitter was selected for spectroscopy, its inclusion in the luminosity function depends on the detection and identification of the Ly α line. Our spectroscopic sensitivity to Ly α emission as a function of flux and redshift is shown in Figure 4; we label this function p_{detect} . As discussed in section § 3.1, p_{detect} can be interpreted as the probability that a putative Ly α emission line of a given flux and a given redshift would have been detected in our spectroscopic campaign.

In the presence of these selection effects, the available volume for a galaxy with Ly α emission of flux $f_{\text{Ly}\alpha}$ is

$$V_{\text{max}} = \int_{z_1}^{z_2} \eta_{\text{try}}(f'_{\text{Ly}\alpha}) p_{\text{detect}}(f'_{\text{Ly}\alpha}, z') \frac{d^2 V_c}{d\Omega dz'} \Delta\Omega dz' , \quad (5)$$

where the comoving volume element in a solid angle $d\Omega$ and redshift interval dz is the familiar

$$\frac{d^2 V_c}{d\Omega dz} = \left(\frac{c}{H_0} \right)^3 \left\{ \int_0^z \frac{dz'}{E(z')} \right\}^2 \frac{1}{E(z)} , \quad (6)$$

with

$$E(z) = \{ \Omega_{\text{M}}(1+z)^3 + \Omega_{\text{k}}(1+z)^2 + \Omega_{\Lambda} \}^{1/2} . \quad (7)$$

In equation 5, $\Delta\Omega$ is the solid angle covered by the LALA survey, and $f'_{\text{Ly}\alpha}$ is the Ly α line flux for the source in question if it were located at redshift z' . The lower limit of integration z_1 is set by the lowest wavelength at which Ly α could be detected by our narrow-band filters, corresponding to $z \approx 4.37$. The upper limit of integration z_2 is set in one of two ways. If the Ly α luminosity for a source is bright enough that the line remains above the survey flux limit out to the highest redshift accessible by our filter set, then z_2 is simply equal to the upper redshift limit for the survey, $z \approx 4.57$. For fainter sources, z_2 is taken to be the redshift at which the Ly α flux falls below the survey flux limit; in this case, $4.37 < z_2 < 4.57$.

Having computed V_{max} for each galaxy, we may compute the differential Ly α luminosity function $\Phi(L)$, the number density of galaxies per logarithmic interval in Ly α luminosity. In a given luminosity bin of width $\Delta \log L$ centered on L_i , this is given by

$$\Phi(L_i) = \frac{1}{\Delta \log L} \sum_j \frac{1}{V_{\text{max},j}}. \quad (8)$$

Here, the index i denotes the luminosity bin and j denotes the galaxies within the bin, where the galaxies summed in a given bin are selected by their Ly α luminosities according to

$$|\log L_j - \log L_i| < \frac{\Delta \log L}{2}. \quad (9)$$

Finally, the uncertainty in the luminosity function may be estimated with

$$\sigma[\Phi(L_i)] = \frac{1}{\Delta \log L} \left[\sum_j \left(\frac{1}{V_{\text{max},j}} \right)^2 \right]^{1/2}. \quad (10)$$

In Figure 10, we present the resulting differential Ly α luminosity function at $z \approx 4.5$. We also fit the data with a Schechter function. If $\Phi(L) dL$ is the comoving number density of galaxies with luminosities in the range $(L, L + dL)$, then the corresponding Schechter function is

$$\Phi(L) dL = \frac{\Phi^*}{L^*} \left(\frac{L}{L^*} \right)^\alpha \exp \left(-\frac{L}{L^*} \right) dL, \quad (11)$$

where Φ^* is the normalization, L^* is the characteristic break luminosity, and α sets the slope at the faint end. This is related to the number density of galaxies in *logarithmic* intervals by

$$\Phi(L) d(\log L) = \left(\frac{L}{\log_{10} e} \right) \left(\frac{\Phi^*}{L^*} \right) \left(\frac{L}{L^*} \right)^\alpha \exp \left(-\frac{L}{L^*} \right) d(\log L),$$

and it is this function which we fit to our data. As in van Breukelen et al. (2005), because the binned data points are few, we choose to fix $\alpha = -1.6$ so as to fit with only two free

parameters, Φ^* and L^* . This choice fits well with the luminosity distribution of both LBGs and Ly α -emitters at $z \approx 3$ (Steidel et al. 1999, 2000). We find best-fit luminosity function parameters $L^* = (10.9 \pm 3.3) \times 10^{42} \text{erg s}^{-1}$ and $\Phi^* = (1.7 \pm 0.2) \times 10^{-4} \text{Mpc}^{-3}$ (or equivalently, $\log(L^*) = 43.04 \pm 0.14$ and $\log(\Phi^*) = -3.77 \pm 0.05$). The error bars on L^* and Φ^* are the 1σ formal errors computed from the covariance matrix in the nonlinear least-squares fit, scaled by the measured value of χ^2 . That is, $\delta L^* = \sigma_{L^*} \sqrt{\chi^2/n_{\text{DOF}}}$, and similarly for $\delta \Phi^*$ (Press et al. 1992).

Our $z \approx 4.5$ sample provides one of the best measured Ly α luminosity functions to date. We can study redshift evolution of the Ly α luminosity function by comparing to results from the literature. Recognizing that the uncertainties in L^* and Φ^* are strongly correlated, we examine not only the individual parameters but also the product $L^*\Phi^*$, which is proportional to Ly α luminosity density, and which generally has smaller uncertainties than the individual parameters. For our sample, $\log(L^*\Phi^*) = 39.27$.

At lower redshift, there is a $z \approx 3.1$ LF by (Gronwall et al. 2007), who fit all three parameters. They find $\alpha = -1.49^{+0.45}_{-0.34}$, $\log(L^*) = 42.64^{+0.26}_{-0.15}$, and $\log(\Phi^*) \approx -2.89 \pm 0.04$, whence $\log(L^*\Phi^*) \approx 39.75$. At the high redshift end, we compare to LFs at $z = 6.5$ by Malhotra & Rhoads (2004) and Kashikawa et al. (2006), and at $z = 5.7$ by Malhotra & Rhoads (2004) and Shimasaku et al. (2006), all derived by fixing the faint end slope $\alpha = -1.5$ and fitting L^* and Φ^* . At $z = 6.5$, the LFs are similar to our $z = 4.5$ result: Malhotra & Rhoads (2004) find $\log(L^*) = 42.6$, $\log(\Phi^*) = -3.3$, and $\log(L^*\Phi^*) = 39.3$, while Kashikawa et al. (2006) find (for their combined spectroscopic + photometric sample) $\log(L^*) = 42.6$, $\log(\Phi^*) = -2.88$, and $\log(L^*\Phi^*) = 39.72$. At $z = 5.7$, Malhotra & Rhoads (2004) find $\log(L^*) = 43.0$, $\log(\Phi^*) = -4.0$, and $\log(L^*\Phi^*) = 39.0$, while Shimasaku et al. (2006) find $\log(L^*) = 42.9 \pm 0.14$, $\log(\Phi^*) = -3.2 \pm 0.17$, and $\log(L^*\Phi^*) = 39.7$. The obvious differences between the LFs at each redshift may be caused by any combination of (a) simple uncertainty in deriving the LF from modest sized samples; (b) field-to-field variations in Ly α galaxy density; or (c) differences in the methods used to derive Schechter function parameters, and in part to local variations in Ly α galaxy density. The Kashikawa et al. (2006) and Shimasaku et al. (2006) LFs are derived from larger total samples, but from a single survey field, while the Malhotra & Rhoads (2004) LFs are based on a combination of several older, smaller samples from a few widely separated fields. Regardless, if we take the difference between these various $z \sim 6$ LFs as an empirical indication of total present uncertainties, the $z \approx 4.5$ LF derived in the present paper supports a roughly constant Ly α luminosity density over the range $z = 4.5 \pm 1.5$.

4.4. Comparison to LBGs

It is interesting to compare this result to the evolution of the rest-UV luminosity density and cosmic star formation rate density (SFRD) derived from LBGs over the same redshift range. Estimates of the $z \approx 6$ SFRD based on the Great Observatories Origins Deep Survey/Advanced Camera for Surveys (GOODS/ACS; Giavalisco et al. 2004a) and the Hubble Ultra Deep Field (Beckwith et al. 2006) show a factor of 1.5–6 drop between $z \sim 3$ and $z \sim 6$ (Bunker et al. 2004; Bouwens et al. 2006; Giavalisco et al. 2004b).

What does this mean for the Ly α -selected galaxies? Steidel et al. (2000) report that Ly α -selection with an equivalent width criterion typical of narrow-band surveys would return 20% – 25% of their $z \approx 3$ LBGs. If Ly α -emitters are merely a subset of the LBG population which happen to have been detected during a stage of strong Ly α production, then we would expect the Ly α luminosity density to decline beyond $z \sim 3$, in step with the global star formation rate density. Integrating the luminosity functions discussed in section 4.3 shows no compelling evidence for such a decline. Though a modest decline cannot be firmly ruled out, we may nonetheless speculate that the Ly α -emitters as a population are evolving differently from the LBGs.

The bolometric luminosities of Ly α galaxies are typically lower than Lyman break galaxies, and provide a hint that they are less massive. Detailed spectral energy distribution fitting (Gawiser et al. 2006; Finkelstein et al. 2007; Pirzkal et al. 2007) bears out this preliminary inference, showing typical masses of $\sim 10^8 M_\odot$ and ages $\sim 10^7$ to 10^8 years. The correlation strengths of Ly α galaxies and LBGs are similar (Ouchi et al. 2003; Kovač et al. 2007), indicating similar masses of haloes. From the expected halo mass one can predict volume number density of Ly α emitters. Comparing the expected and observed number densities implies a duty cycle of Ly α -emission in the range 6% – 50% (Kovač et al. 2007). A similar duty cycle, 7.5% - 15%, is inferred from stellar population modelling of the photometric sample (Malhotra & Rhoads 2002).

4.5. Implications for Reionization

The spectroscopic observations of the $z > 6$ quasars yielded the first detections of the long-awaited Gunn-Peterson trough, implying at least the end of reionization at $z \approx 6$ (Becker et al. 2001; Djorgovski et al. 2001; Fan et al. 2002). Subsequently, the *Wilkinson Microwave Anisotropy Probe* (WMAP) identified a large amplitude signal in the temperature-polarization maps of the cosmic microwave background (Spergel et al. 2003; Page et al. 2006) indicating a large optical depth to Thomson scattering and favoring reionization instead at

$z \approx 11$. The WMAP results are not necessarily inconsistent with those of the quasar Gunn-Peterson troughs. Only a small neutral fraction ($x_{\text{HI}}^{\text{IGM}} \sim 0.001$) is required to produce the Gunn-Peterson effect, so one plausible scenario is that reionization may have been an extended event, beginning early but not completing until $z \approx 6$. Alternatively, a variety of theoretical models now suggest that reionization occurred twice, first at $z \approx 20$ with the onset of zero-metallicity Population III stars, and then again by massive Population II stars formed after a partial recombination (e.g., Cen 2003; Haiman & Holder 2003; Somerville et al. 2003).

High-redshift Ly α -emitting galaxies offer another perspective on this issue, as the visibility of Ly α emission should be a sensitive function of the IGM neutral fraction (e.g., Haiman & Spaans 1999; Santos 2004). Malhotra & Rhoads (2004) and Stern et al. (2005) present first attempts to exploit this fact by comparing luminosity functions of Ly α -emitters at $z \sim 5.7$ and $z \sim 6.6$. They find no measurable evolution between these epochs, from which they infer that the IGM remains largely reionized from the local universe out to $z \approx 6.5$ (but see Haiman & Cen 2005). Kashikawa et al. (2006), applying the same test, find possible evidence for observed Ly α LF differences between $z = 5.7$ and 6.5 at the factor of 2 level. They suggest neutral gas at $z \approx 6.5$ as the explanation, though Dijkstra et al. (2007) argue that the observations could equally well be explained by the ongoing growth of cosmic structure from $z = 6.5$ to $z = 5.7$.

By using the Ly α galaxy sample from Taniguchi et al. (2005), Malhotra & Rhoads (2006) showed that at least 30% of the IGM by volume is ionized at $z \approx 6.5$. This is corroborated by dark gap statistics in GP troughs (Fan et al. 2006). All the Ly α tests of reionization assume that there is no intrinsic evolution in the Ly α luminosity functions between $z = 5.7$ and 6.5 . In this paper we show that there is little evolution in Ly α luminosity function from $z = 6.6$ to $z = 3.1$, thus strengthening the conclusion that the IGM is not substantially neutral at $z = 6.5$.

Significantly, the related question of *what* is responsible for reionization remains at large. It has long been recognized that AGN at early epochs are insufficient, owing to their rapid decline in space density at high redshift (e.g., Madau et al. 1999; Barger et al. 2003). Based on their analysis of the UDF, Bunker et al. (2004) conclude that the cosmic SFR in directly observed $z \approx 6$ LBGs was roughly five times too low to reionize the Universe. Yan & Windhorst (2004) and Bouwens et al. (2006) argue that the ionizing photon budget is sufficient provided one accounts for sample incompleteness using a sufficiently steep slope at the faint end of the luminosity function. Malhotra et al. (2005) argue that the ionizing flux density may be very inhomogeneous due to large scale structure, as seen in galaxies in the Hubble Ultra Deep Field, and that the directly observed galaxies at $z \approx 6$ do produce sufficient photons for reionization in overdense regions.

We estimate that the contribution to the cosmic SFR from Ly α -emitters at this epoch is lower than that of the LBGs ($\rho_{\text{SFR}}(\text{Ly}\alpha) \approx 0.003 M_{\odot} \text{ yr}^{-1} \text{ Mpc}^{-3}$, as compared to $\rho_{\text{SFR}}(\text{LBG}) \approx 0.005 M_{\odot} \text{ yr}^{-1} \text{ Mpc}^{-3}$) when integrated over the same limits. Consequently, though high-redshift Ly α -emitters are proving to be a useful probe of the history of reionization, they are evidently not its cause. While extinction corrections could occasionally be large (Chary et al. 2005) and could modify this conclusion, most well studied Ly α galaxies have very modest extinction (Finkelstein et al. 2007; Pirzkal et al. 2007).

When we compare the luminosity function of Ly α -emitters at $z \approx 4.5$ to luminosity functions for similarly assembled samples spanning $3.1 < z < 6.6$, we find no evidence for evolution over these epochs. This result bolsters the conclusion by Malhotra & Rhoads (2004) and Stern et al. (2005) that the IGM remains largely reionized from the local universe out to $z \approx 6.5$. However, it is somewhat at odds with the factor of 1.5–6 drop in the cosmic star formation rate density measured by (Bunker et al. 2004; Bouwens et al. 2006; Giavalisco et al. 2004a) between $z \sim 3$ and $z \sim 6$ in Lyman-break galaxies selected in the exceptional imaging of the UDF. It seems that these two populations— Ly α emitters and Lyman Break Galaxies— follow different evolutionary histories. The disentanglement of this issue will likely rely on extensive followup observations of large samples, so that we can study the continuum and absorption lines of many Ly α galaxies, and conversely the Ly α properties of the break-selected galaxies.

This work benefited greatly from conversations with M. Cooper, S. McCarthy, T. Robshaw, and J. Simon, as well as from the careful commentary of the anonymous referee. In addition, we are humbly indebted to the expert staff of W. M. Keck Observatory for their assistance in obtaining the data herein. It is a pleasure to thank P. Amico, J. Lyke, and especially G. Wirth for their invaluable assistance during observing runs. We thank F. Valdes for writing the “deitab” package, which aids in DEIMOS data processing. Finally, we wish to acknowledge the significant cultural role that the summit of Mauna Kea plays within the indigenous Hawaiian community; we are fortunate to have the opportunity to conduct observations from this mountain. This material is based upon work supported by AURA through the National Science Foundation under AURA Cooperative Agreement AST 0132798 as amended. The work of D. S. was carried out at the Jet Propulsion Laboratory, California Institute of Technology, under contract with NASA. A. D. and B. J. acknowledge support from NOAO, which is operated by the Association of Universities for Research in Astronomy, Inc., under cooperative agreement with the National Science Foundation (NSF). H. S. gratefully acknowledges NSF grant AST 95-28536 and its successors for supporting much of the research presented herein. This work made use of NASA’s Astrophysics Data System Abstract Service.

REFERENCES

- Ajiki, M. et al. 2002, *ApJ*, 576, L25
- . 2003, *AJ*, 126, 2091
- Ando, M., Ohta, K., Iwata, I., Watanabe, C., Tamura, N., Akiyama, M., & Aoki, K. 2004, *ApJ*, 610, 635
- Barger, A. J., Cowie, L. L., Capak, P., Alexander, D. M., Bauer, F. E., Fernandez, E., Brandt, W. N., Garmire, G. P., & Hornschemeier, A. E. 2003, *AJ*, 126, 632
- Becker, R. H. et al. 2001, *AJ*, 122, 2850
- Beckwith, S. V. W., et al. 2006, *AJ*, 132, 1729
- Bouwens, R. J. et al. 2003, *ApJ*, 595, 589
- . 2004, *ApJ*, 616, L79
- . 2004, *ApJ*, accepted, astro-ph/0509641
- Bunker, A. J., Stanway, E. R., Ellis, R. S., & McMahon, R. G. 2004, American Astronomical Society Meeting Abstracts, 204,
- Cen, R. 2003, *ApJ*, 591, 12
- Charlot, S. & Fall, S. M. 1993, *ApJ*, 415, 580
- Chary, R. R., Stern, D., Eisenhardt, P. 2005, *ApJ*, 635, L5
- Cowie, L. L. & Hu, E. M. 1998, *AJ*, 115, 1319
- Cuby, J.-G., Le Fèvre, O., McCracken, H., Cuillandre, J.-C., Magnier, E., & Meneux, B. 2003, *A&A*, 405, L19
- Davis, M. et al. 2003, in Discoveries and Research Prospects from 6- to 10-Meter-Class Telescopes II. Edited by Guhathakurta, Puragra. Proceedings of the SPIE, Volume 4834, pp. 161-172 (2003)., 161–172
- Dawson, S., McCrady, N. Stern, D., Eckart, M., Spinrad, H., Liu, M., & Graham, J. 2003, *AJ*, 125, 1236
- Dawson, S., Spinrad, H., Stern, D., Dey, A., van Breugel, W., de Vries, W., & Reuland, M. 2002, *ApJ*, 570, 92

- Dawson, S., Stern, D., Bunker, A. J., Spinrad, H., & Dey, A. 2001, *AJ*, 122, 598
- Dawson, S. et al. 2004, *ApJ*, 617, 707 (Paper I)
- Dey, A., Spinrad, H., Stern, D., Graham, J. R., & Chaffee, F. H. 1998, *ApJ*, 498, L93
- Dickinson, M. et al. 2004, *ApJ*, 600, L99
- Dijkstra, M., Wyithe, S., & Haiman, Z. 2007, *MNRAS*, in press; astro-ph/0611195
- Djorgovski, S. G., Castro, S., Stern, D., & Mahabal, A. A. 2001, *ApJ*, 560, L5
- Ellis, R., Santos, M. R., Kneib, J., & Kuijken, K. 2001, *ApJ*, 560, L119
- Faber, S. M. et al. 2003, *Proc. SPIE*, 4841, 1657
- Fan, X. et al. 2006, *AJ*, submitted
- Fan, X., Narayanan, V. K., Strauss, M. A., White, R. L., Becker, R. H., Pentericci, L., & Rix, H. 2002, *AJ*, 123, 1247
- Fan, X. et al. 2001, *AJ*, 121, 54
- Finkelstein, S. L., Rhoads, J. E., Malhotra, S., Pirzkal, N., & Wang, J. X. 2007, *ApJ* 660, 1023
- Fujita, S. S. et al. 2003, *AJ*, 125, 13
- Gawiser, E., et al. 2006, *ApJ*, 642, L13
- Giavalisco, M. et al. 2004a, *ApJ*, 600, L93
- . 2004b, *ApJ*, 600, L103
- Gronwall, C. et al. 2007, *ApJ*, in press; astro-ph/0705.3917
- Haiman, Z. & Spaans, R. 1999, *ApJ*, 518, 138
- Haiman, Z. & Cen, R. 2005, *ApJ*, 623, 627
- Haiman, Z. & Holder, G. P. 2003, *ApJ*, 595, 1
- Hogg, D. W., Cohen, J. G., Blandford, R., & Pahre, M. A. 1998, *ApJ*, 504, 622
- Horne, K. 1986, *PASP*, 98, 609

- Hu, E. M., Cowie, L. L., Capak, P., McMahon, R. G., Hayashino, T., & Komiyama, Y. 2004, *AJ*, 127, 563
- Hu, E. M., Cowie, L. L., & McMahon, R. G. 1998, *ApJ*, 502, L99
- Hu, E. M., Cowie, L. L., McMahon, R. G., Capak, P., Iwamuro, F., Kneib, J.-P., Maihara, T., & Motohara, K. 2002, *ApJ*, 568, L75
- Iwata, I., Ohta, K., Tamura, N., Ando, M., Wada, S., Watanabe, C., Akiyama, M., & Aoki, K. 2003, *PASJ*, 55, 415
- Jannuzi, B. T. & Dey, A. 1999, in *ASP Conf. Ser. 191, Photometric Redshifts and High Redshift Galaxies*, ed. R. J. Weymann, L. J. Storrie-Lombardi, M. Sawicki, & R. J. Brunner (San Francisco: ASP), 111
- Kashikawa, N. et al., 2006, *ApJ*, 648, 7
- Kodaira, K. et al. 2003, *PASJ*, 55, L17
- Kovač, K., Somerville, R. S., Rhoads, J. E., Malhotra, S., & Wang, J. X. 2007, *ApJ*, in press; astro-ph/0706.0893.
- Kudritzki, R.-P. et al. 2000, *ApJ*, 536, 19
- Lehnert, M. D. & Bremer, M. 2003, *ApJ*, 593, 630
- Lowenthal, J. D., Koo, D. C., Guzman, R., Gallego, J., Phillips, A. C., Faber, S. M., Vogt, N. P., Illingworth, G. D., & Gronwall, C. 1997, *ApJ*, 481, 673
- Madau, P. 1995, *ApJ*, 441, 18
- Madau, P., Ferguson, H. C., Dickinson, M. E., Giavalisco, M., Steidel, C. C., & Fruchter, A. 1996, *MNRAS*, 283, 1388
- Madau, P., Haardt, F., & Rees, M. J. 1999, *ApJ*, 514, 648
- Maier, C., Meisenheimer, K., Thommes, E., Hippelein, H., Röser, H. J., Fried, J., von Kuhlmann, B., Phleps, S., & Wolf, C. 2003, *A&A*, 402, 79
- Malhotra, S. & Rhoads, J. E. 2002, *ApJ*, 565, L71
- . 2004, *ApJ*, 617, L5
- Malhotra, S. et al 2006

- . 2006, ApJ, submitted.
- Malhotra, S., Wang, J. X., Rhoads, J. E., Heckman, T. M., & Norman, C. A. 2003, ApJ, 585, L25
- Manning, C., Stern, D., Spinrad, H., & Bunker, A. J. 2000, ApJ, 537, 65
- Massey, P. & Gronwall, C. 1990, ApJ, 358, 344
- Mo, H. J., Mao, S., & White, S. D. M. 1998, MNRAS, 295, 319
- Nagao, T. et al. 2004, ApJ, 613, L9
- Neufeld, D. A. 1991, ApJ, 370, 85
- Norman, C. et al. 2002, ApJ, 571, 218
- Oke, J. B., Cohen, J. G., Carr, M., Cromer, J., Dingizian, A., Harris, F. H., Labrecque, S., Lucinio, R., Schaal, W., Epps, H., & Miller, J. 1995, PASP 107, 375
- Ouchi, M. et al. 2003, ApJ, 582, 600
- Ouchi, M. et al. 2004, ApJ, 611, 660
- Page, L. et al. 2006, ApJ, submitted
- Pirzkal, N., Malhotra, S., Rhoads, J. E., & Xu, C. 2007, ApJ, in press; astro-ph/0612513
- Press, W. H., Teukolsky, S. A., Vetterling, W. T., & Flannery, B. P. 1992, Numerical Recipes in C: The Art of Scientific Computing, 2nd edn. (Cambridge University Press)
- Rhoads, J. E. & Malhotra, S. 2001, ApJ, 563, L5
- Rhoads, J. E., Malhotra, S., Dey, A., Stern, D., Spinrad, H., & Jannuzi, B. T. 2000, ApJ, 545, L85
- Rhoads, J. E. et al. 2003, ApJ, 125, 1006
- . 2004, ApJ, 611, 59
- Santos, M. R. 2004, MNRAS, 349, 1137
- Scannapieco, E., Schneider, R., & Ferrara, A. 2003, ApJ, 589, 35
- Shimasaku, K. et al. 2006, PASJ, 58, 313

- Somerville, R. S., Bullock, J. S., & Livio, M. 2003, *ApJ*, 593, 616
- Spergel, D. N. et al. 2003, *ApJS*, 148, 175
- Spinrad, H., Stern, D., Bunker, A., Dey, A., Lanzetta, K., Yahil, A., Pascarelle, S., & Fernández-Soto, A. 1998, *AJ*, 116, 2617
- Stanway, E. R., Bunker, A. J., & McMahon, R. G. 2003, *MNRAS*, 342, 439
- Stanway, E. R., Bunker, A. J., McMahon, R. G., Ellis, R. S., Treu, T., & McCarthy, P. J. 2004a, *ApJ*, 607, 704
- Stanway, E. R. et al. 2004b, *ApJ*, 604, L13
- Steidel, C. C., Adelberger, K. L., Giavalisco, M., Dickinson, M., & Pettini, M. 1999, *ApJ*, 519, 1
- Steidel, C. C., Adelberger, K. L., Shapley, A. E., Pettini, M., Dickinson, M., & Giavalisco, M. 2000, *ApJ*, 532, 170
- Steidel, C. C., Giavalisco, M., Pettini, M., Dickinson, M., & Adelberger, K. L. 1996, *ApJ*, 462, L17
- Stern, D., Bunker, A., Spinrad, H., & Dey, A. 2000, *ApJ*, 537, 73
- Stern, D. & Spinrad, H. 1999, *PASP*, 111, 1475
- Stern, D., Yost, S. A., Eckart, M. E., Harrison, F. A., Helfand, D. J., Djorgovski, S. G., Malhotra, S., & Rhoads, J. E. 2005, *ApJ*, 619, 12
- Stern, D. et al. 2002, *ApJ*, 568, 71
- Taniguchi, Y. et al. 2003, *ApJ*, 585, L97
- . 2005, *PASJ*, 57, 165
- Tody, D. 1993, in *ASP Conf. Ser. 52, Astronomical Data Analysis Software and Systems II*, ed. R. Hanisch, R. Brissenden, & J. Barnes (San Francisco: ASP), 173
- van Breukelen, C., Jarvis, M. J., & Venemans, B. P. 2005, *MNRAS*, 359, 895
- Wang, J. X. et al. 2004, *ApJ*, 608, L21
- Weymann, R. J., Stern, D., Bunker, A., Spinrad, H., Chaffee, F. H., Thompson, R. I., & Storrie-Lombardi, L. J. 1998, *ApJ*, 505, L95

Yan, H. & Windhorst, R. A. 2004, ApJ, 612, L93

Yan, H., Windhorst, R. A., & Cohen, S. H. 2003, ApJ, 585, L93

Yan, H. et al. 2005, ApJ, in press [astro-ph/0507673]

Zhang, Y., Anninos, P., Norman, M. L., & Meiksin, A. 1997, ApJ, 485, 496

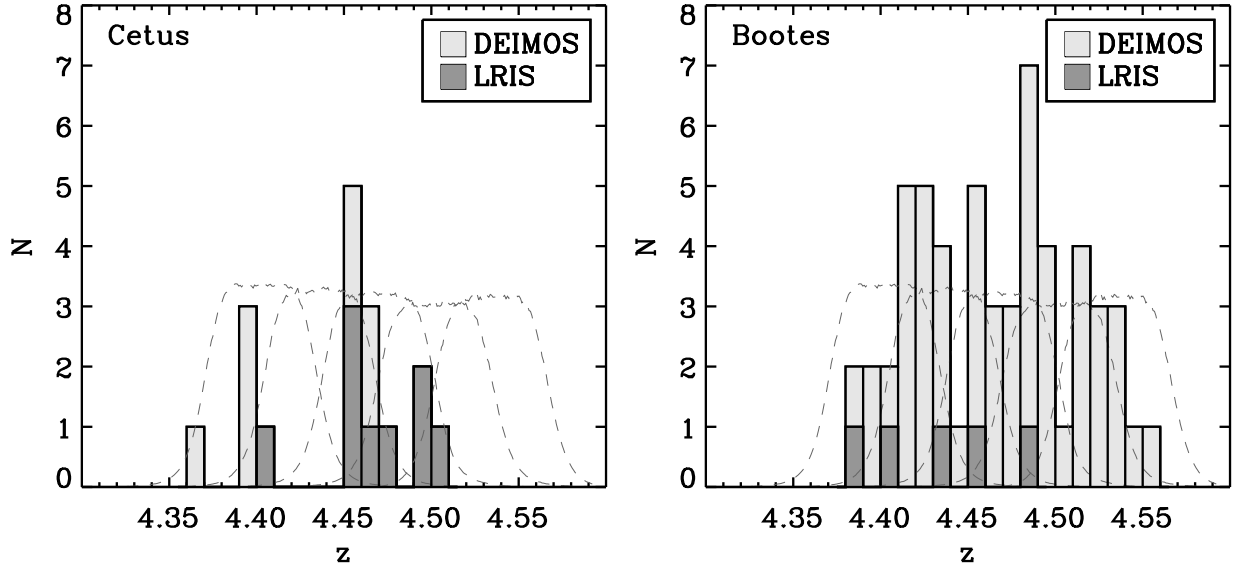


Fig. 1.— Distribution of redshifts for spectroscopically confirmed $\text{Ly}\alpha$ emission lines in the Cetus field (left; 02:05:20 –04:55, J2000.0) and in the Boötes field (right; 14:25:57 +35:32, J2000.0). The redshifts labeled “DEIMOS” denote galaxies confirmed with our campaign of Keck/DEIMOS spectroscopy, described in this paper. The redshifts labeled “LRIS” denote galaxies confirmed with our campaign of Keck/LRIS spectroscopy, described in Paper I. The overlays are arbitrarily scaled transmission curves for the five narrow-band filters employed in the imaging component of this survey.

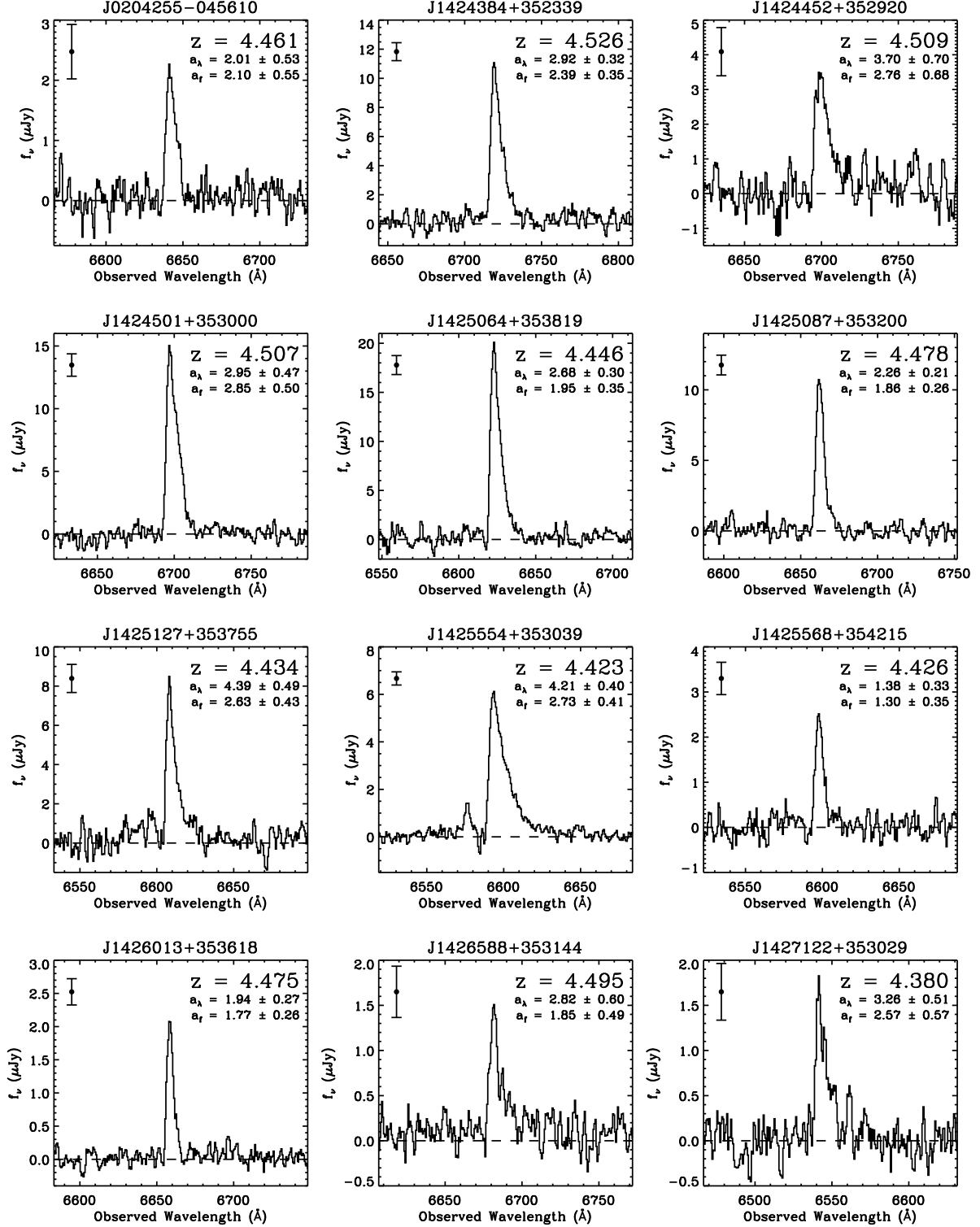


Fig. 2.— Sample spectra from the set of 59 $z \approx 4.5$ Ly α -emitting galaxies confirmed with Keck/DEIMOS, with a wavelength range selected to highlight the emission-line profile. The measured redshifts and asymmetry statistics (§ 3.2) are indicated in the upper right of each panel. The representative error bar (*upper left*) is the median of the flux error in each pixel over the wavelength range displayed. The spectra have been smoothed with a 3-pixel boxcar average.

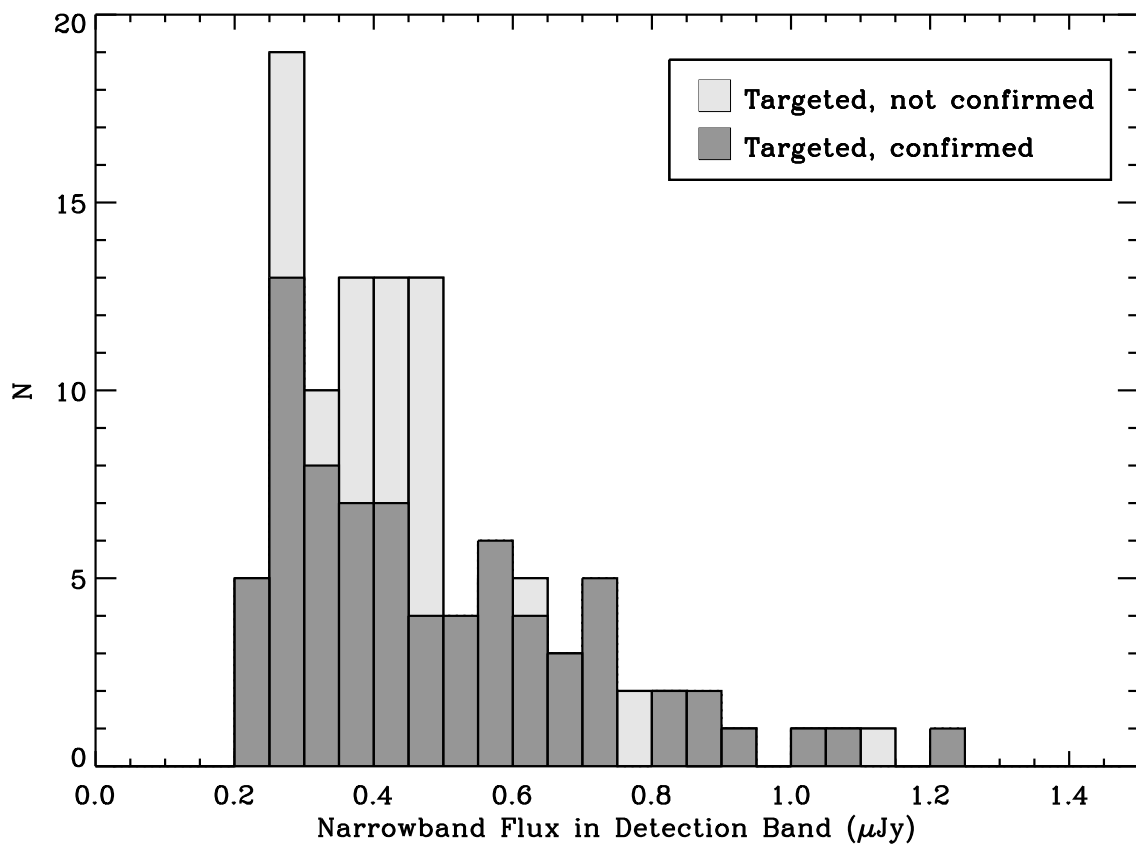


Fig. 3.— Spectroscopic success rate as a function of the flux in the narrow-band in which the candidate was selected. This plot combines the results of the Keck/DEIMOS observations made for this paper and the Keck/LRIS observations described in Paper I.

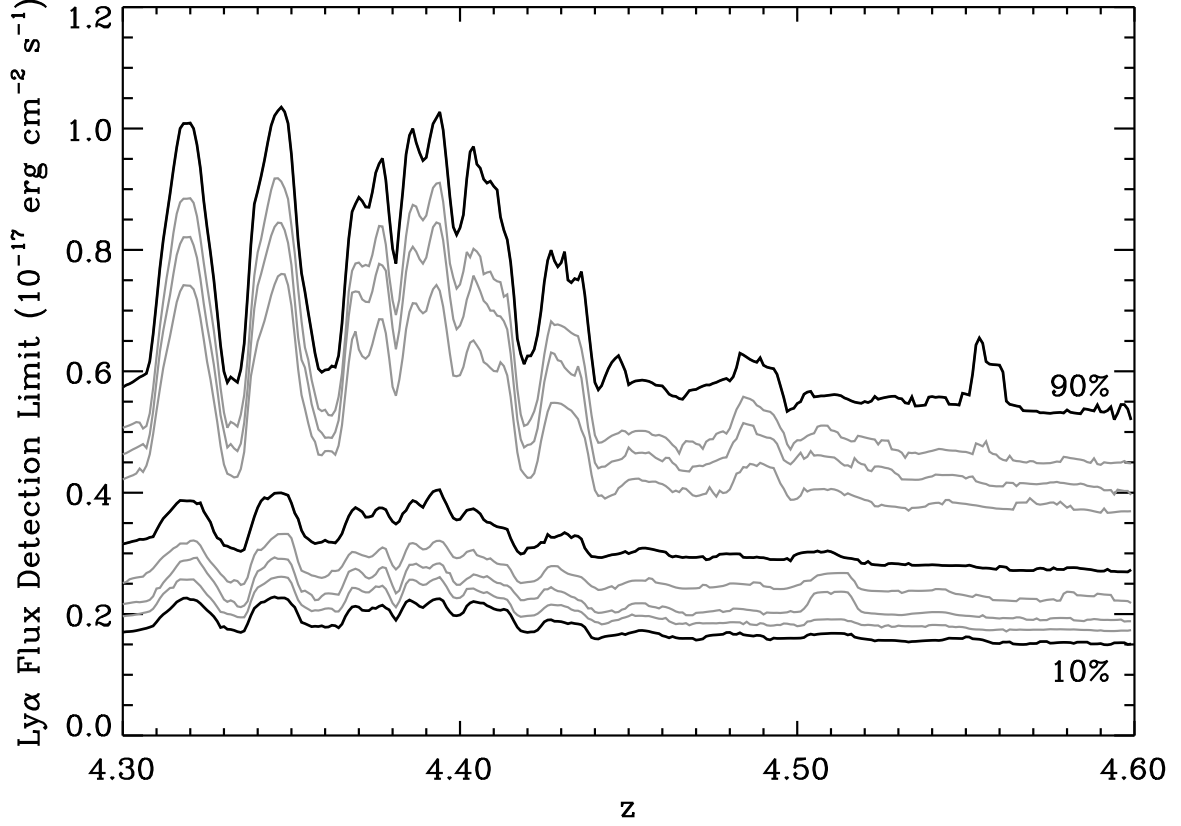


Fig. 4.— Empirical, cumulative distribution of spectroscopic sensitivity to Ly α emission, as a function of source redshift and Ly α flux. The contours span 10% to 90% in 10% steps. The dark lines denote the 10%, 50%, and 90% contours. The distribution is plotted cumulatively so that it can be interpreted as the probability that a putative Ly α emission line of a given flux and redshift would have been detected in our Keck/DEIMOS spectroscopic campaign.

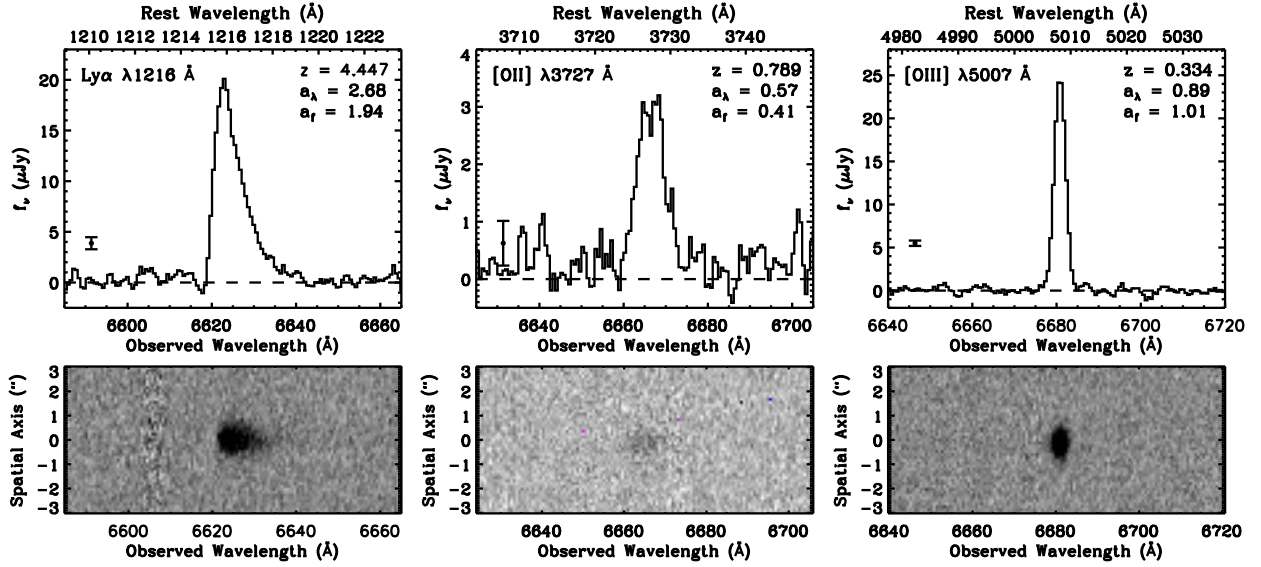


Fig. 5.— Sample Ly α emission line profile (*left*) compared to two common low-redshift interlopers: [O II] λ 3727 (*center*) and [O III] λ 5007 (*right*). The top figure in each case is the one-dimensional extracted spectrum; the bottom figure is a section of the two-dimensional data from which it was extracted. Note that we resolve the [O II] λ 3727 doublet with our Keck/DEIMOS spectroscopic setup, thereby eliminating [O II] λ 3727 as the main low-redshift interloper in our survey. The [O III] λ 5007 line can typically be identified by neighboring [O III] λ 4959 at one-third its strength, or by neighboring H β .

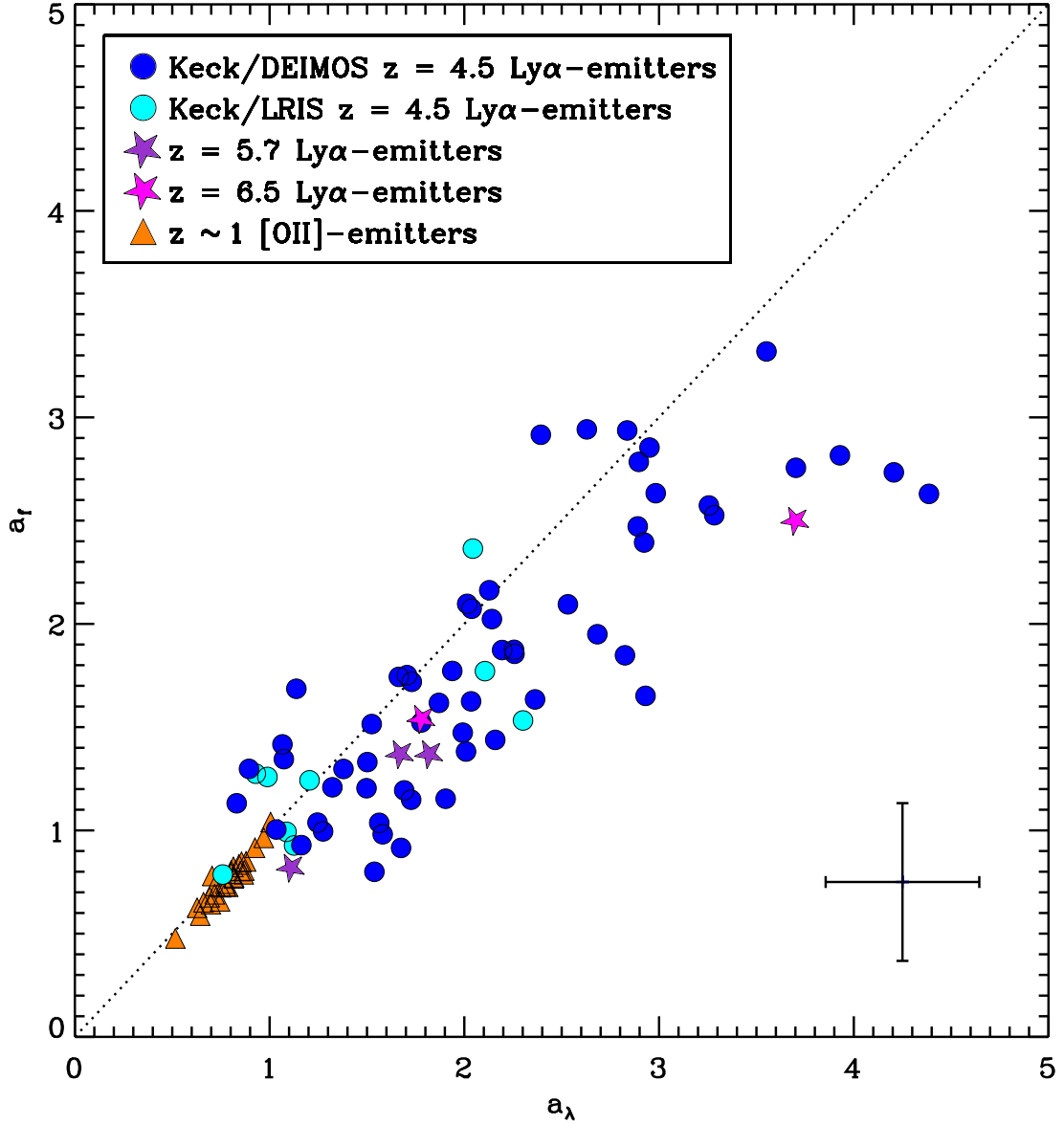


Fig. 6.— Scatter plot comparing the flux-based asymmetry statistic a_f and the wavelength-based asymmetry statistic a_λ of known high-redshift Ly α -emitters to a sample of [O II] $\lambda 3727$ -emitters at $z \sim 1$, updated from Paper I. The points labeled “DEIMOS” denote galaxies confirmed with our campaign of Keck/DEIMOS spectroscopy, described in this paper. The points labeled “LRIS” denote galaxies confirmed with our campaign of 400 ℓ /mm-grating Keck/LRIS spectroscopy, described in Paper I. The three Ly α -emitters at $z = 5.7$ are from Rhoads et al. (2003), and the two Ly α -emitters at $z = 6.5$ are from Rhoads et al. (2004) and Stern et al. (2005). The 28 [O II] $\lambda 3727$ -emitters at $z \sim 1$ were provided by the DEEP2 team (Davis et al. 2003, A. Coil 2004, private communication); their Keck/DEIMOS 1200 ℓ /mm-grating spectra were smoothed to the Keck/LRIS 400 ℓ /mm-grating resolution by convolution with a Gaussian kernel. The representative error bar (*lower right*) is the median of the errors on the individual a_f and a_λ for the combined Keck/LRIS and Keck/DEIMOS sample.

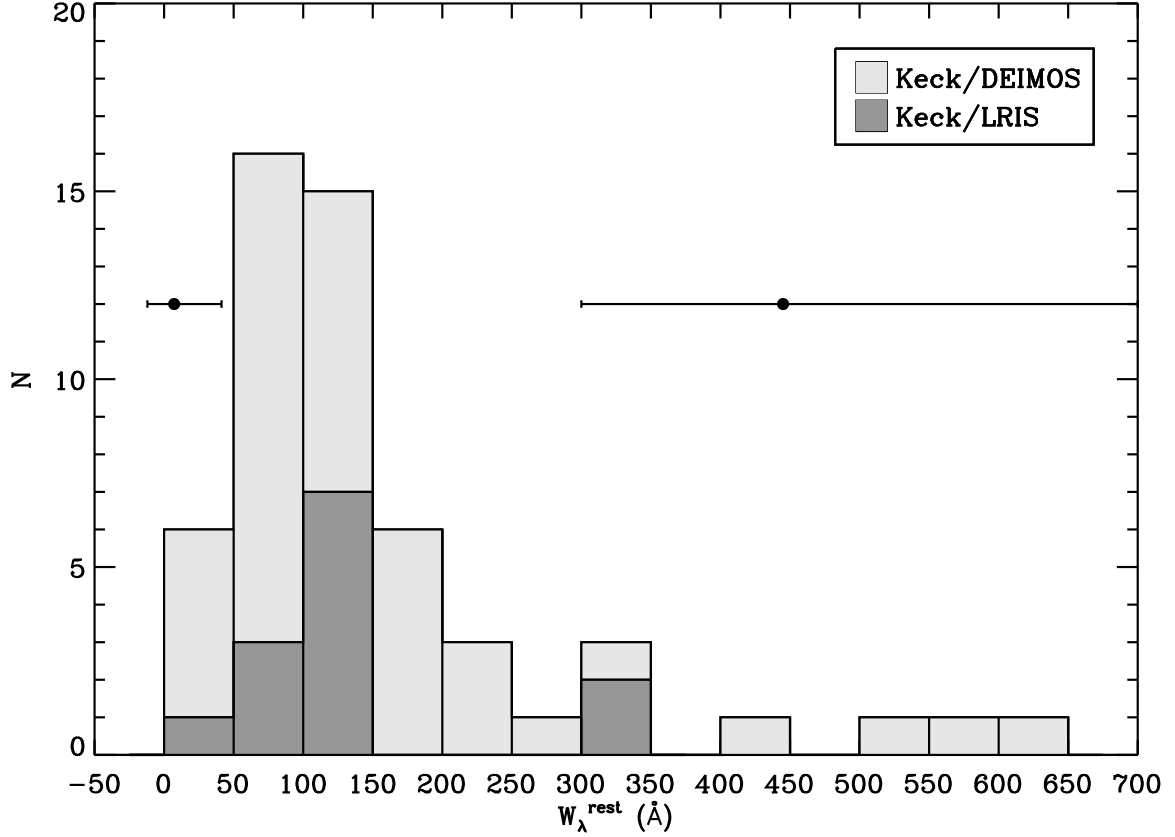


Fig. 7.— Histogram of the spectroscopic rest-frame equivalent widths for the $z = 4.5$ population, determined with $W_{\lambda}^{\text{rest}} = (F_{\ell}/f_{\lambda,r})/(1+z)$, where F_{ℓ} is the flux in the emission line and $f_{\lambda,r}$ is the measured red-side continuum flux density. The sources labeled “DEIMOS” denote galaxies confirmed with our campaign of Keck/DEIMOS spectroscopy, described in this paper. The sources labeled “LRIS” denote galaxies confirmed with our campaign of Keck/LRIS spectroscopy, described in Paper I. Representative error bars on the equivalent widths are plotted at left and at right. Notably, the highest equivalent widths are generally the least certain, as they correspond to the faintest (and hence least certain) continuum estimates.

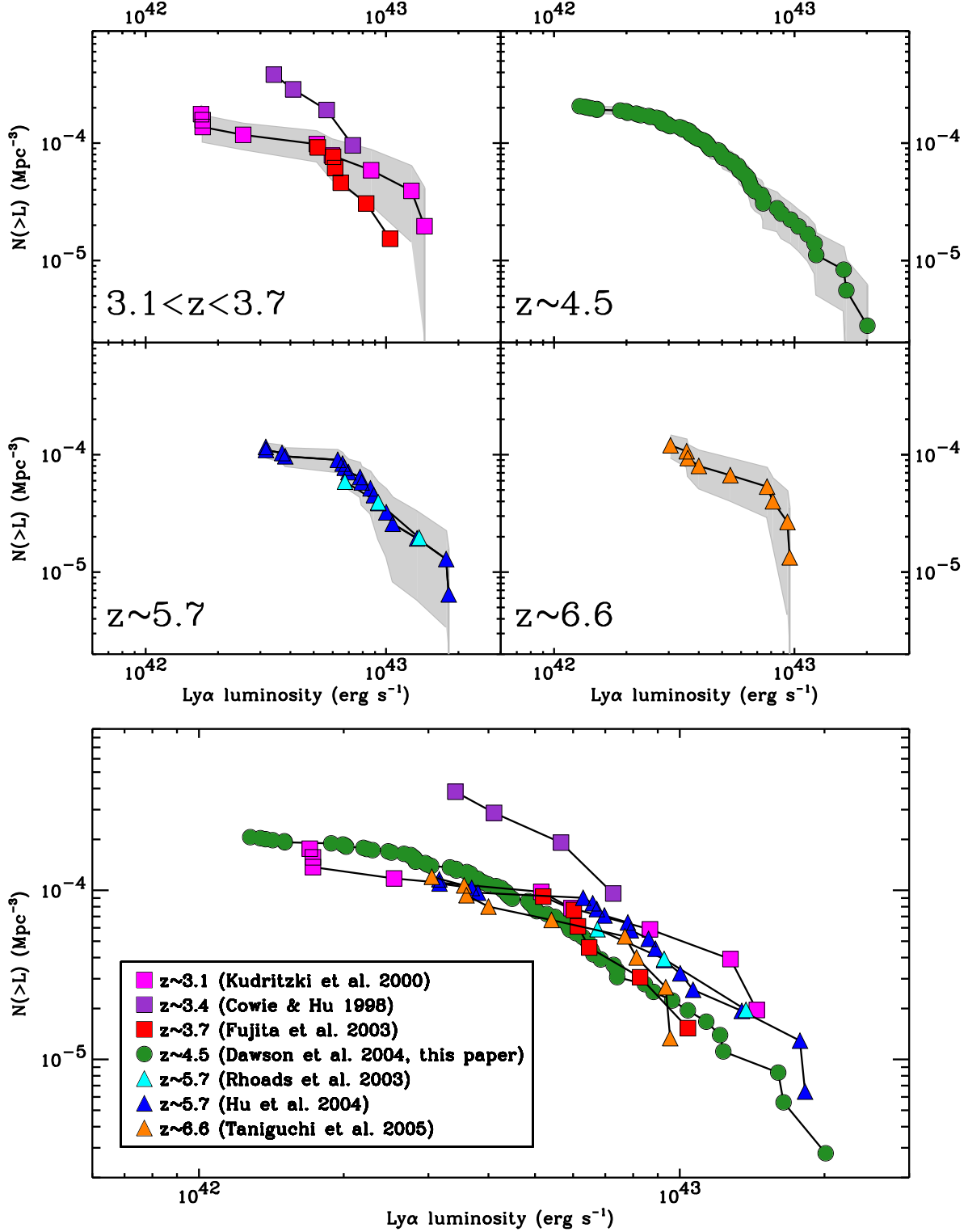


Fig. 8.— Comparison of empirical, cumulative Ly α luminosity functions computed with only minimal completeness correction for several spectroscopic surveys spanning $3.1 < z < 6.6$. The cumulative luminosity function gives for each Ly α line luminosity $L(\text{Ly}\alpha)$ the total number density of Ly α lines brighter than $L(\text{Ly}\alpha)$. The shaded regions represent 95% confidence intervals based on the Monte Carlo simulations described in § 4.2. Where more than one survey is plotted, just the confidence intervals for the survey with the largest range in line fluxes is depicted. No strong evolution is evident over the redshift range depicted.

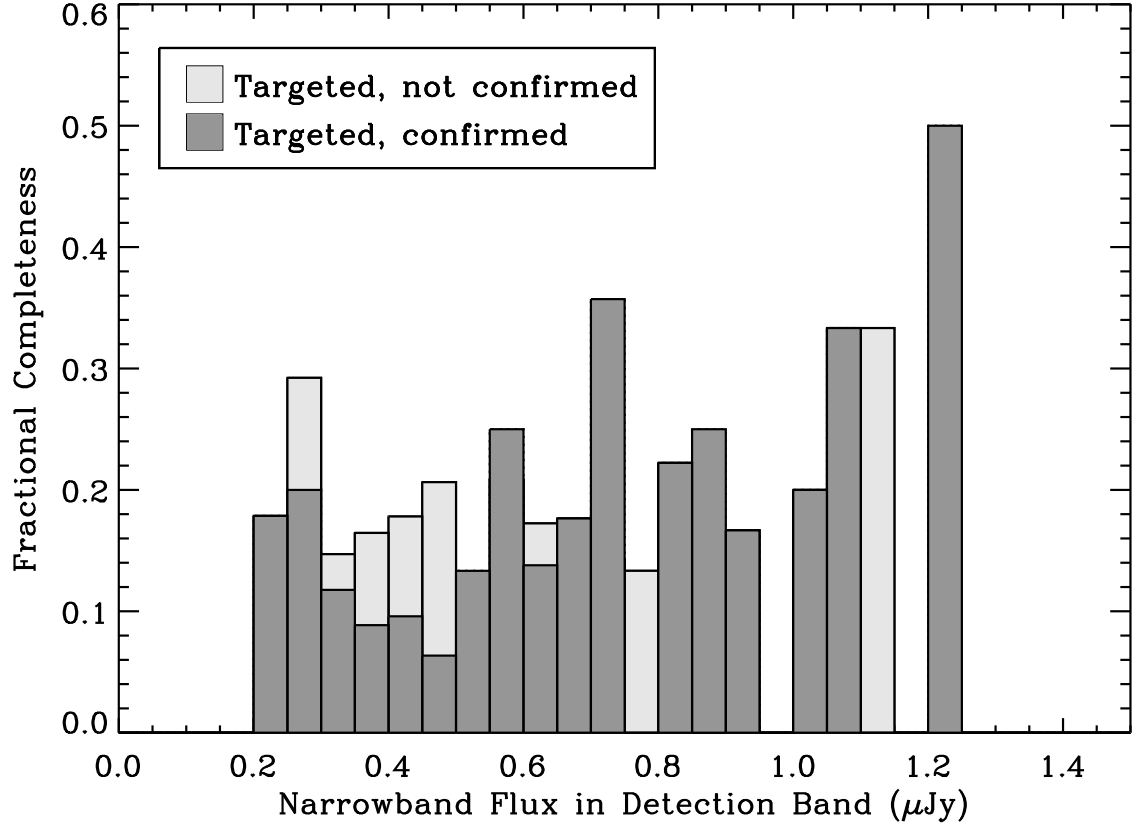


Fig. 9.— Probability as a function of narrow-band flux that a candidate $\text{Ly}\alpha$ -emitter was targeted for spectroscopy, divided into the fraction of targets that were confirmed and the fraction of targets that were not.

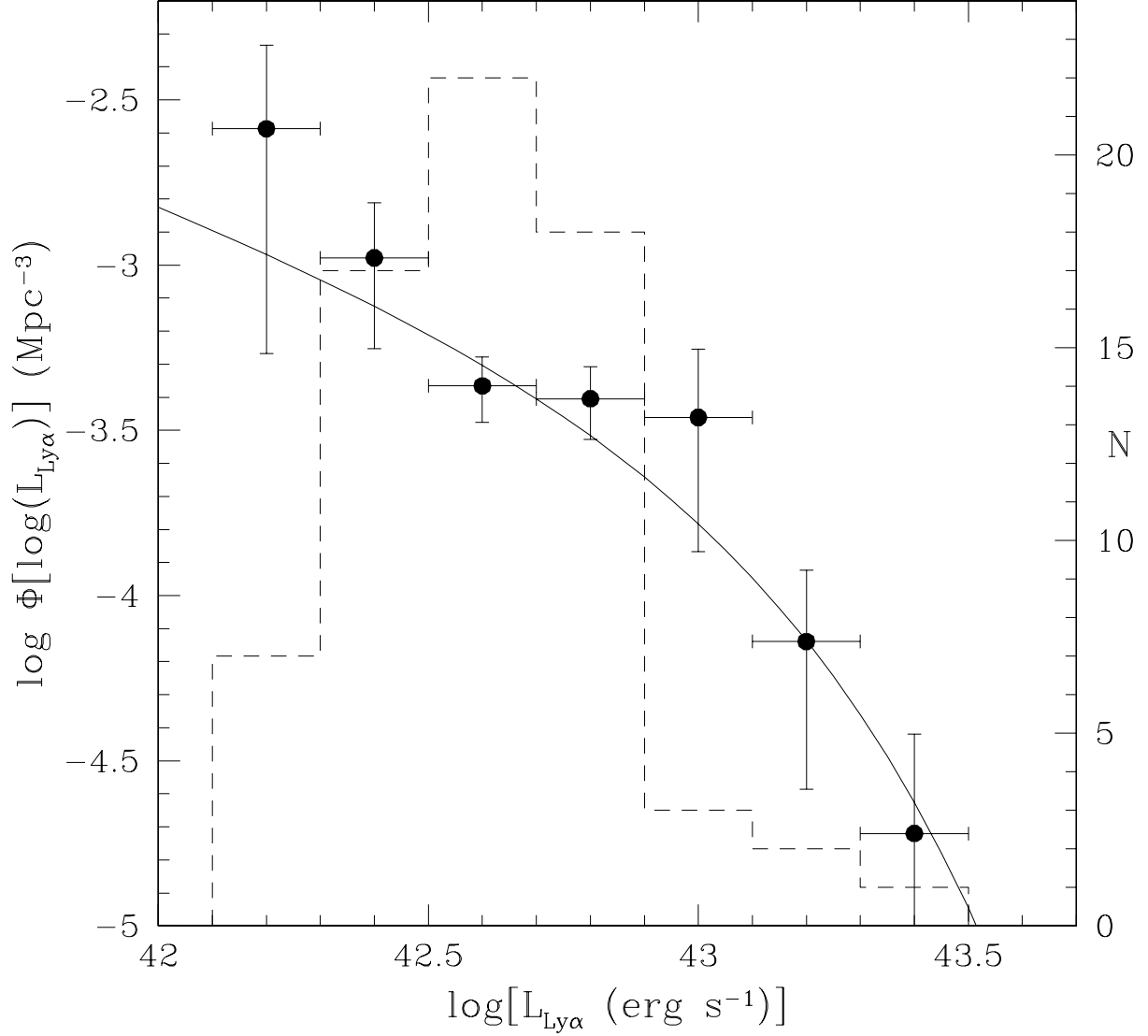


Fig. 10.— Differential Ly α luminosity function for our $z = 4.5$ sample, computed using the V/V_{max} method. The sample includes both the Keck/DEIMOS data presented in this paper and the Keck/LRIS data presented in Paper I. The error bars are the 1σ statistical uncertainties given by the root variance shown in equation 10. The background histogram (dashed) gives the number of individual sources contributing to each luminosity bin. The solid curve shows the best fitting Schechter function model, with $L^* = (10.9 \pm 3.3) \times 10^{42}$ erg s $^{-1}$, $\Phi^* = (1.7 \pm 0.2) \times 10^{-4}$ Mpc $^{-3}$, and a fixed faint-end slope $\alpha = -1.6$.

Table 1. Spectroscopic Properties

Target	z^a	Ly α Flux ^b (10^{-17} erg cm $^{-2}$ s $^{-1}$)	$W_{\lambda}^{\text{restc}}$ (\AA)	FWHM ^d (\AA)	Δv^e (km s $^{-1}$)	Continuum (μJy) ^f Blue Side	Continuum (μJy) ^f Red Side
J020418.2–050748	4.449	2.55 ± 0.87	$> 86^g$	6.8 ± 1.7	230	-0.040 ± 0.026	-0.018 ± 0.049
J020423.2–050647	4.449	3.25 ± 1.07	$> 108^g$	5.7 ± 1.0	160	-0.003 ± 0.026	0.014 ± 0.034
J020425.5–045610	4.461	3.72 ± 1.22	379^{+2092}_{-187}	7.2 ± 1.0	260	0.002 ± 0.025	0.026 ± 0.031
J020425.7–045810	4.387	1.98 ± 0.68	$> 39^g$	4.1 ± 0.6	$< 200^h$	-0.035 ± 0.052	0.021 ± 0.057
J020427.4–050045	4.390	1.47 ± 0.54	$> 142^g$	5.4 ± 2.8	140	-0.010 ± 0.018	-0.011 ± 0.019
J020428.5–045924	4.390	3.57 ± 1.27	508^{+4493}_{-278}	11.0 ± 2.8	460	-0.008 ± 0.032	0.019 ± 0.033
J020429.8–050251	4.460	1.39 ± 0.52	$> 22^g$	7.1 ± 2.2	250	-0.124 ± 0.070	0.012 ± 0.077
J020432.3–045519	4.360	3.13 ± 1.04	$> 241^g$	4.2 ± 1.3	$< 210^h$	-0.003 ± 0.023	-0.009 ± 0.022
J142434.9+352833	4.423	1.13 ± 0.46	26^{+30}_{-12}	6.8 ± 1.1	230	0.037 ± 0.077	0.117 ± 0.073
J142436.0+352600	4.464	1.81 ± 0.72	38^{+17}_{-16}	5.0 ± 0.2	100	0.016 ± 0.022	0.128 ± 0.025
J142438.4+352339	4.526	3.21 ± 1.28	26^{+11}_{-10}	7.0 ± 0.5	240	0.175 ± 0.036	0.336 ± 0.061
J142445.2+352920	4.509	1.21 ± 0.49	9^{+4}_{-3}	9.5 ± 1.5	370	0.106 ± 0.041	0.350 ± 0.049
J142445.3+352450	4.475	2.47 ± 0.99	$> 55^g$	5.6 ± 0.3	150	-0.056 ± 0.043	-0.009 ± 0.065
J142445.4+352859	4.514	0.98 ± 0.40	6^{+2}_{-2}	8.2 ± 2.0	310	0.174 ± 0.040	0.447 ± 0.052
J142450.1+353000	4.507	4.32 ± 1.73	83^{+70}_{-36}	8.2 ± 0.6	310	-0.010 ± 0.050	0.141 ± 0.063
J142452.4+352613	4.411	1.97 ± 0.79	97^{+212}_{-46}	6.5 ± 0.6	210	0.051 ± 0.038	0.054 ± 0.047
J142458.6+353558	4.522	2.02 ± 1.06	$> 24^g$	5.6 ± 0.5	150	-0.026 ± 0.078	-0.006 ± 0.116
J142459.8+353927	4.482	1.98 ± 1.05	$> 59^g$	5.0 ± 0.5	100	0.030 ± 0.041	-0.009 ± 0.049
J142501.7+353652	4.496	1.38 ± 0.78	43^{+721}_{-24}	6.4 ± 2.0	200	0.073 ± 0.100	0.088 ± 0.140
J142502.8+353017	4.476	0.75 ± 0.31	$> 20^g$	5.6 ± 0.9	150	0.052 ± 0.034	0.016 ± 0.042
J142503.4+353222	4.489	0.66 ± 0.28	21^{+18}_{-9}	4.1 ± 2.2	$< 200^h$	0.113 ± 0.037	0.086 ± 0.044
J142506.4+353819	4.446	8.11 ± 4.26	594^{+4407}_{-336}	7.0 ± 0.3	250	0.008 ± 0.054	0.037 ± 0.065
J142508.3+353952	4.511	2.59 ± 1.36	175^{+844}_{-93}	8.6 ± 0.6	330	-0.019 ± 0.038	0.040 ± 0.048
J142508.7+353200	4.478	2.41 ± 0.96	$> 75^g$	6.0 ± 0.4	180	0.032 ± 0.040	-0.010 ± 0.049
J142512.0+353913	4.451	1.13 ± 0.60	$> 30^g$	4.1 ± 1.4	$< 200^h$	0.063 ± 0.040	0.000 ± 0.050
J142512.7+353755	4.434	2.96 ± 1.56	34^{+19}_{-17}	6.1 ± 0.6	190	0.201 ± 0.040	0.235 ± 0.053
J142518.0+353415	4.408	5.37 ± 2.15	39^{+18}_{-15}	8.7 ± 0.8	340	0.150 ± 0.062	0.370 ± 0.072
J142522.4+353553	4.519	1.79 ± 0.72	39^{+30}_{-16}	7.4 ± 0.6	260	0.011 ± 0.046	0.126 ± 0.053
J142525.9+352349	4.471	3.27 ± 1.34	33^{+16}_{-13}	7.0 ± 0.7	240	0.072 ± 0.048	0.267 ± 0.057
J142526.2+352531	4.464	2.76 ± 1.13	85^{+105}_{-39}	6.2 ± 0.4	190	0.067 ± 0.050	0.087 ± 0.054
J142531.8+352652	4.482	0.94 ± 0.40	18^{+9}_{-7}	7.4 ± 1.5	270	0.034 ± 0.035	0.140 ± 0.041
J142532.9+353013	4.534	5.49 ± 1.00	201^{+75}_{-51}	7.1 ± 0.3	250	0.005 ± 0.015	0.075 ± 0.018
J142535.2+352743	4.449	6.23 ± 2.54	159^{+173}_{-72}	6.0 ± 0.2	180	0.001 ± 0.048	0.106 ± 0.057
J142539.5+353902	4.432	1.52 ± 0.67	240^{+2182}_{-126}	4.0 ± 1.6	$< 200^h$	0.049 ± 0.019	0.017 ± 0.022
J142541.7+353351	4.409	3.24 ± 1.34	108^{+139}_{-50}	5.4 ± 0.8	130	-0.042 ± 0.045	0.080 ± 0.050
J142542.0+352557	4.393	1.05 ± 0.44	30^{+28}_{-13}	6.4 ± 1.4	210	0.028 ± 0.033	0.092 ± 0.042
J142542.6+352626	4.450	1.49 ± 0.62	19^{+10}_{-7}	7.5 ± 0.9	270	0.101 ± 0.043	0.215 ± 0.059
J142544.5+354325	4.533	2.84 ± 1.20	131^{+129}_{-60}	7.4 ± 1.1	260	0.002 ± 0.018	0.059 ± 0.030
J142546.8+354315	4.443	0.72 ± 0.33	40^{+34}_{-19}	6.3 ± 1.5	200	0.012 ± 0.016	0.049 ± 0.022
J142547.8+354200	4.539	1.11 ± 0.48	$> 56^g$	4.9 ± 0.8	90	0.029 ± 0.017	0.007 ± 0.024
J142548.4+352740	4.546	1.21 ± 0.50	$> 24^g$	5.4 ± 0.7	130	-0.058 ± 0.038	0.004 ± 0.067
J142555.4+353039	4.423	10.31 ± 1.88	560^{+467}_{-190}	10.8 ± 0.6	450	0.025 ± 0.015	0.049 ± 0.023
J142556.7+354234	4.425	2.26 ± 0.96	189^{+284}_{-89}	4.8 ± 0.6	80	-0.019 ± 0.020	0.032 ± 0.022
J142556.8+354215	4.426	2.85 ± 1.20	162^{+152}_{-74}	5.8 ± 0.7	170	0.021 ± 0.020	0.047 ± 0.022
J142559.8+353513	4.394	1.39 ± 0.28	158^{+189}_{-60}	5.6 ± 0.6	160	0.005 ± 0.013	0.023 ± 0.014

Table 1—Continued

Target	z^a	Ly α Flux ^b (10^{-17} erg cm $^{-2}$ s $^{-1}$)	$W_{\lambda}^{\text{rest c}}$ (\AA)	FWHM ^d (\AA)	Δv^e (km s $^{-1}$)	Continuum (μJy) ^f Blue Side	Continuum (μJy) ^f Red Side
J142559.8+353748	4.420	4.95 ± 0.91	55^{+10}_{-10}	7.0 ± 0.5	240	0.109 ± 0.018	0.240 ± 0.019
J142601.3+353618	4.475	1.41 ± 0.27	$> 171^g$	5.0 ± 0.4	100	-0.013 ± 0.011	-0.003 ± 0.013
J142602.0+354554	4.473	1.83 ± 0.78	85^{+70}_{-38}	4.8 ± 0.7	70	-0.003 ± 0.019	0.058 ± 0.025
J142612.2+353541	4.418	1.90 ± 0.36	$> 140^g$	6.3 ± 0.5	200	0.082 ± 0.013	0.002 ± 0.017
J142624.4+353832	4.460	2.46 ± 0.46	320^{+1182}_{-145}	5.4 ± 0.5	140	-0.012 ± 0.017	0.021 ± 0.022
J142627.5+353717	4.488	2.11 ± 0.43	42^{+24}_{-14}	6.5 ± 2.4	210	0.044 ± 0.025	0.135 ± 0.051
J142628.5+353809	4.409	3.82 ± 0.71	$> 143^g$	6.4 ± 0.4	210	-0.038 ± 0.029	-0.011 ± 0.041
J142653.5+353356	4.494	2.12 ± 0.77	142^{+115}_{-59}	7.8 ± 1.8	280	-0.016 ± 0.015	0.040 ± 0.017
J142658.8+353144	4.495	2.16 ± 0.79	31^{+11}_{-10}	6.3 ± 1.0	200	-0.019 ± 0.015	0.191 ± 0.018
J142706.3+353224	4.480	0.99 ± 0.38	100^{+139}_{-45}	5.0 ± 1.6	100	0.021 ± 0.014	0.027 ± 0.018
J142709.1+352738	4.407	1.77 ± 0.65	85^{+50}_{-34}	8.4 ± 1.4	320	0.039 ± 0.014	0.056 ± 0.017
J142709.2+352409	4.520	1.62 ± 0.59	$> 85^g$	5.8 ± 1.2	170	0.029 ± 0.015	0.008 ± 0.022
J142709.8+352641	4.405	1.78 ± 0.66	178^{+337}_{-82}	6.0 ± 0.8	180	0.023 ± 0.017	0.027 ± 0.021
J142712.2+353029	4.380	2.35 ± 0.86	82^{+45}_{-32}	4.3 ± 2.4	$< 200^h$	0.035 ± 0.017	0.076 ± 0.021

^aThe redshift was derived from the wavelength of the peak pixel in the line profile smoothed with a 3-pixel boxcar average. We estimate the error in this measurement to be $\delta z \approx 0.0005$, based on Monte Carlo simulations in which we added random noise to each pixel of every spectrum according to the photon counting statistics, and then re-measured the redshift in each case. This measurement may overestimate the true redshift of the system since the blue wing of the Ly α emission is absorbed by foreground neutral hydrogen.

^bThe line flux was determined by totaling the flux of the pixels that fall within the line profile. No attempt was made to model the emission line or to account for the very minor contribution of the continuum to the line. Quoted uncertainties account for photon counting errors alone, excluding possible systematic errors. Despite these caveats, the Ly α line fluxes measured from the spectra agree with narrow band imaging to 1σ in all but three cases.

^cThe rest frame equivalent widths were determined with $W_{\lambda}^{\text{rest}} = (F_{\ell}/f_{\lambda,r})/(1+z)$, where F_{ℓ} is the flux in the emission line and $f_{\lambda,r}$ is the measured red-side continuum flux density. The error bars δw_+ and δw_- are 1σ confidence intervals determined by integrating over the probability density functions $P_i(w)$ described in § 4.1. The error bars are symmetric in probability density-space in the sense that $\int_{w-\delta w_-}^w P_i(w') dw' = \int_w^{w+\delta w_+} P_i(w') dw' = 0.34$.

^dThe FWHM was measured directly from the emission line by counting the number of pixels in the unsmoothed spectrum which exceed a flux equal to half the flux in the peak pixel. No attempt was made to account for the minor contribution of the continuum to the height of the peak pixel. The error bars were determined with Monte Carlo simulations in which we modeled each emission line with the truncated Gaussian profile described in Hu et al. (2004) and Rhoads et al. (2004), added random noise in each pixel according to the photon counting errors, and then measured the widths $\sigma(\text{FWHM})$ of the resulting distribution of FWHM for the given line.

^eThe velocity width Δv was determined by subtracting in quadrature the effective instrumental resolution for a point source, and is therefore an upper limit, as the target may have angular size comparable to the $\lesssim 1''$ seeing of these data. Where the emission line is unresolved, the velocity width is an upper limit set by the effective width of the resolution element itself.

^fRed and blue side continuum measurements are variance-weighted averages made in 1200 \AA wide windows beginning 30 \AA from the wavelength of the peak pixel in the emission line. We employed a 10-iteration, 2σ clipping algorithm to reduce the effect of spurious outliers occurring at long wavelength, where the sky noise is large. In some cases, a small correction factor was subtracted from the variance-weighted averages based on the detection of residual signal remaining in extractions of source-free, sky-subtracted regions of the two-dimensional spectra (see text, § 2.2). Quoted uncertainties account for photon counting errors in the source extractions added in quadrature to the photon counting errors derived in the blank-sky extractions.

^g 2σ lower limit. The measurement of the red-side continuum for this source is formally consistent with no observable flux. The equivalent width limit was then set by using a 2σ upper limit to $f_{\lambda,r}$ in the expression given in footnote (c).

^hThis line is unresolved.